Three-dimensional, nonhydrostatic numerical simulation of nonlinear internal wave generation and propagation in the South China Sea

Z. Zhang,[1] O. B. Fringer,[1] and S. R. Ramp[2]

Received 24 May 2010; revised 24 January 2011; accepted 23 February 2011; published 27 May 2011.

[1] We present the results of three-dimensional, nonhydrostatic simulations of internal tides and waves in the South China Sea (SCS) using the SUNTANS model. Model results accurately predict the observed wave arrival times at two mooring locations in the SCS. Internal wave amplitudes are underpredicted which causes underprediction of internal wave speeds due to a lack of amplitude dispersion. We show that the well-known A and B waves arise from the steepening of semidiurnal internal tides that are generated due to strong barotropic flow over ridges in the Luzon Strait. A wave generation is stronger in the southern portion of the Luzon Strait because diurnal internal tidal beams augment the amplitude of the semidiurnal A waves. B wave generation is stronger in the northern portion where the distance between the eastern and western ridges is approximately equal to one internal tidal wavelength and leads to semidiurnal internal tidal resonance. The orientation of the ridges produces large A waves that propagate into the northern portion of the western SCS basin and stronger B waves that propagate into the southern portion. When traced back in time along linear characteristics, A waves consistently line up close to peak ebb (eastward) barotropic currents, while B waves consistently line up with peak flood (westward) barotropic currents. This reinforces the notion that the lee wave mechanism and associated hydraulic or nonlinear effects are weak, as demonstrated by a simple linear model relating the amplitude of the simulated waves to the excursion parameter at the ridges.

Citation: Zhang, Z., O. B. Fringer, and S. R. Ramp (2011), Three-dimensional, nonhydrostatic numerical simulation of nonlinear internal wave generation and propagation in the South China Sea, *J. Geophys. Res.*, *116*, C05022, doi:10.1029/2010JC006424.

1. Introduction

[2] Internal gravity waves are generated when ocean tidal currents interact with bottom topography, resulting in internal tides, or internal waves of tidal frequency, that propagate throughout the world's oceans. Internal gravity waves are visible from space through alterations in surface wave behavior, and satellite imagery indicates that internal waves exist in almost every corner of the globe. Upon formation, internal tides have wavelengths of tens to hundreds of kilometers, amplitudes of tens to hundreds of meters, and propagate at speeds of 2–4 m s^{-1} depending on water depth and stratification. If the amplitude upon generation is large enough, internal gravity waves can disperse into trains of weakly nonlinear solitary-like waves. Like surface waves, internal gravity waves diffract and refract around topography and, upon encountering shallow water, a decrease in wavelength is accompanied by an increase in amplitude, which ultimately leads to breaking.

[3] Among the largest internal gravity waves are those observed in the South China Sea (hereinafter referred to as SCS; see Figure 1). Evidence for the existence of these large-amplitude and thus nonlinear internal gravity waves has been primarily obtained by satellite imagery [*Jackson and Apel*, 2004; *Liu et al.*, 2004], and in situ observations [*Ramp et al.*, 2004, 2010; *Duda et al.*, 2004; *Alford et al.*, 2010; *Lien et al.*, 2005; *Farmer et al.*, 2009]. Most of the observed nonlinear internal waves (NLIW) appear as tidally periodic groups that are widely recognized to originate from topography in the Luzon Strait because of the irregular topography and enhanced tidal currents there. Generation sites have been determined primarily from three-dimensional simulations of internal tides and calculations of the energy flux which indicate primary generation along the eastern Luzon Ridge. Secondary, weaker generation occurs along the western Heng-Chun ridge [*Zhang and Fringer*, 2006; *Niwa and Hibiya*, 2004; *Jan et al.*, 2008]. The western ridge has been shown to have the potential to reduce the magnitude of westward propagating internal wave energy by *Chao et al.* [2007]. *Buijsman et al.* [2010a] showed that the western

[1]Environmental Fluid Mechanics Laboratory, Department of Civil and Environmental Engineering, Stanford University, Stanford, California, USA.
[2]Monterey Bay Aquarium Research Institute, Moss Landing, California, USA.

0148-0227/11/2010JC006424

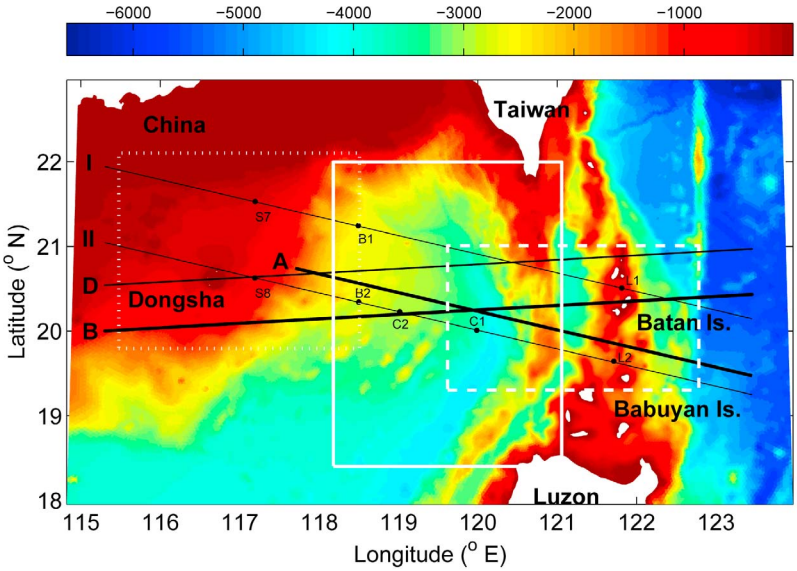

Figure 1. Bathymetry of the SCS (in m), showing the locations of mooring sites L1, B1, and S7 deployed in the 2005 WISE/VANS experiment [*Ramp et al.*, 2010]. Locations C1, C2, L2, B2, and S8 are referred to in the text but do not have corresponding observations. Transects A, B, D, and I and II are also referred to in the text. The white boxes indicate regions shown in detail in Figures 8 (dotted), 10 (solid), and 20 (dashed).

ridge can amplify westward propagating waves owing to resonance of the semidiurnal internal tide.

[4] Two prominent mechanisms exist for the possible generation mechanism of waves in the SCS. The first is the lee wave hydraulic mechanism of *Maxworthy* [1979], which has been validated by a number of soliton observations and numerical models [e.g., *Liu et al.*, 1985; *Lansing and Maxworthy*, 1984; *Apel et al.*, 1985; *Farmer and Smith*, 1980]. In the Luzon Strait, *Ramp et al.* [2004] hypothesize that this lee wave mechanism may occur when lee waves of depression form on the eastern side of the Batan Islands during the ebb (eastward) tide, and these are "released" westward into the SCS upon reversal of the tidal currents. The waves then evolve into trains of weakly NLIW as they propagate toward the Chinese continent. Using numerical simulations with an idealized two-layer model, *Cai et al.* [2002] show that nonlinear internal waves in the SCS can evolve from the lee wave mechanism which occurs in a narrow channel between Batan and Sabtang Islands. Observations of *Ramp et al.* [2010] indicate peak displacements of the isotherm at mooring B1 on the western side of the SCS basin (see Figure 1) correspond to peaks of eastward tidal currents near the Batan islands. This suggests that the internal waves observed in the western SCS basin are generated during strong ebb tides at the Batan Islands 33 h earlier, which is the time it takes for the first-mode internal tide to propagate from the Batan Islands to where it is observed in the basin. The observations also suggest that the amplitude of the NLIWs is correlated with the spring-neap variability of the tidal currents, such that the largest waves emerge during spring tides. Observations also indicate that seasonal effects result in weak or no waves during the weakly stratified winter.

[5] A second possible generation mechanism is the nonlinear internal tide mechanism. In this mechanism, an internal tide initially generated due to barotropic flow over topography is steepened and then forms an internal solitary wave packet under the effects of nonlinearity and dispersion, as demonstrated by *Zhao and Alford* [2006]. Using satellite observations and numerical model results, *Lien et al.* [2005] hypothesize that packets of nonlinear internal waves in the SCS evolve from the nonlinear steepening of the baroclinic tides and not necessarily from waves generated by the lee wave mechanism. Using a two-dimensional hydrostatic model, *Du et al.* [2008] discuss two possible generation mechanisms, namely the evolution of a depression wave formed during flood tide, which is similar to the internal tide mechanism, and the evolution of a disturbance resulting from internal vertical mixing. Using two-dimensional nonhydrostatic ROMS, *Buijsman et al.* [2010b] suggest that rather than evolving from lee waves of depression, westward propagating solitons form on the backside of an elevation wave lifted by the eastward tidal currents on the west side of the ridge followed by a depression wave on the subsequent westward tide. The internal tide mechanism is also demonstrated to be a likely candidate for the observed nonlinear waves in the SCS by *Farmer et al.* [2009]. They use the weakly nonlinear two-layer model of *Gerkama* [1996] to reproduce observations of nonlinear steepening west of the western Heng-Chun ridge. Using the breaking criterion of *Boyd* [1995], Farmer et al. show that purely semidiurnal internal tides "break", or evolve into trains of solitary waves at 120.3°E, which is close to the longitude of 120.5°E east of which no waves are observed in satellite imagery [*Liu and Hsu*, 2004; *Jackson*, 2009]. Using a three-dimensional nonhydrostatic model, *Shaw et al.* [2009] indicate that both lee waves and internal tides play a role in the internal solitary wave (ISW) generation. The ridge slope determines the occurrence of linear internal tide generation, while lee waves contribute the energy needed to form nonlinear ISWs.

[6] The complexity of the generation mechanism and the physics that govern subsequent propagation and evolution into trains of weakly NLIW are further complicated by superposition of waves from numerous sources along the ridges in the Luzon Strait. Superposition of first-mode waves generates complex interference patterns like those in the vicinity of the Hawaiian Ridge [*Rainville et al.*, 2010]. Internal wave beams can form attractors leading to strengthening of the internal wave signal between multiple sources (P. Echeverri et al., Internal tide attractors in double ridge systems, submitted to *Journal of Fluid Mechanics*, 2010). The waves that are generated in the SCS are also influenced by the Kuroshio intrusion which results in westward propagating internal wave shoaling at a thermocline that is deeper on the eastern side of the Luzon Strait than on the western side [*Buijsman et al.*, 2010a]. Horizontal shear due to the Kuroshio may also steer the westward propagating internal tide [*Kunze*, 1985], and Kuroshio-induced cross-ridge subtidal flow can affect the generation process. *Cai et al.* [2002] show that a mean westward current reduces the amplitude of the eastward propagating waves. *Buijsman et al.* [2010b] showed that the amplitude of westward propagating solitons depends on the difference between the peak eastward and westward currents rather than the magnitude of the subtidal current.

[7] Simulation of NLIW in the SCS is difficult because the waves are highly multiscale. They propagate over hundreds of kilometers, yet their wavelengths range from hundreds of kilometers near their origin down to hundreds of meters after they disperse into trains of solitary-like waves. Upon reaching the shelf, the waves transform into still shorter waves. These short waves dissipate their energy through breaking at submeter scales. This multiscale behavior necessitates a large amount of computational resources if a broad range of scales is to be captured. As an example, *Barad and Fringer* [2010] showed that three-dimensional simulation of shear instabilities in a single solitary-like wave with a wavelength of 500 m requires three weeks using 1024 processors. Internal solitary-like waves are influenced by both rotational [*Helfrich*, 2007] and nonhydrostatic dispersion, the latter of which requires extensive computational resources because of the requirement to compute a three-dimensional elliptic Poisson equation for the nonhydrostatic pressure. This elliptic equation can double the computation time [*Fringer et al.*, 2006] of an already prohibitively large computational problem. The computational difficulties are further compounded by the sensitivity of the results to the stratification, which can vary seasonally and spatially due to the Kuroshio intrusion. Furthermore, resolution of the bathymetry has been shown to strongly affect internal wave amplitude [*Jachec et al.*, 2006]. Due to the many complexities associated with simulation of NLIW in the SCS, the aforementioned modeling studies have been limited to two-dimensional (both hydrostatic and nonhydrostatic) simulations over idealized single- or double-ridged topography. While three-dimensional simulations have been performed, most have been hydrostatic and employed on relatively coarse grids. Coarse grids suffice if the primary concern is to calculate internal wave energetics to assess generation sites.

[8] Recently, H. L. Simmons and L. St. Laurent (Dynamic modeling of tidally generated internal waves in the South China Sea, manuscript in preparation, 2010) performed high-resolution (1/64th degree), three-dimensional hydrostatic simulations with observed stratification and bathymetry, and these simulations capture the nonlinear behavior of the NLIW and yield excellent predictive capability. Similar hydrostatic simulations have been performed using the Northern South China Sea Nowcast/Forecast System [*Chapman et al.*, 2004], and this framework enables inclusion of the Kuroshio current. While these simulations capture a bulk of the physics, they are hydrostatic. To this end, in this paper we present simulation results using the nonhydrostatic SUNTANS model [*Fringer et al.*, 2006] which we apply in three dimensions with the observed bathymetry, stratification and tides. The objective is to understand the generation mechanisms and sources of the internal tides and waves that are observed in the SCS. Section 2 introduces the setup using the SUNTANS model, and in section 3 the results are validated with remote sensing imagery and in situ observations of barotropic tides and temperature profiles. In section 4 we describe detailed model results to help identify generation sites and to understand the mechanisms governing the generation and propagation physics. We summarize and draw conclusions in section 5.

2. Methodology

2.1. The SUNTANS Model

[9] To simulate the generation and propagation of NLIW in the SCS, we employ the parallel, unstructured grid, nonhydrostatic ocean model SUNTANS [*Fringer et al.*, 2006]. The SUNTANS model solves the three-dimensional Navier-Stokes equation under the Boussinesq approximation on a finite volume grid which is unstructured in plan and structured in the vertical. The free surface is advanced semi-implicitly to avoid stability limitations associated with fast free surface gravity waves (which can be as fast as 243 m s^{-1} in the SCS). A projection method is used, whereby the hydrostatic solution is obtained first. The hydrostatic solution is then updated with the nonhydrostatic pressure in a way that locally conserves volume at each time step. A two-dimensional elliptic equation results from the free surface discretization, and a three-dimensional elliptic equation results from the nonhydrostatic pressure projection method. We employ a high-resolution total variation diminishing (TVD) scheme [*Harten*, 1983] with the Superbee limiter [*Roe*, 1985] for advection of the temperature and salinity fields. This results in low numerical diffusion and is essential for the simulation of NLIW (see *Zhang* [2010] for details).

2.2. Model Setup

[10] Simulations are performed in the domain shown in Figure 1 over the period 17 June to 2 July 2005, a time in which extensive internal wave activity is observed [*Ramp et al.*, 2010]. The bathymetry data were obtained from Ocean Data Bank of the National Center for Ocean Research, Taiwan, with a resolution of 1 arc min (~1800 m). The boundaries of the model are forced with the first eight tidal current components from the OTIS global tidal model [*Egbert and Erofeeva*, 2002]. At all open boundaries, a 50 km wide sponge layer is imposed to absorb the internal waves that may reflect back into the domain. The sponge

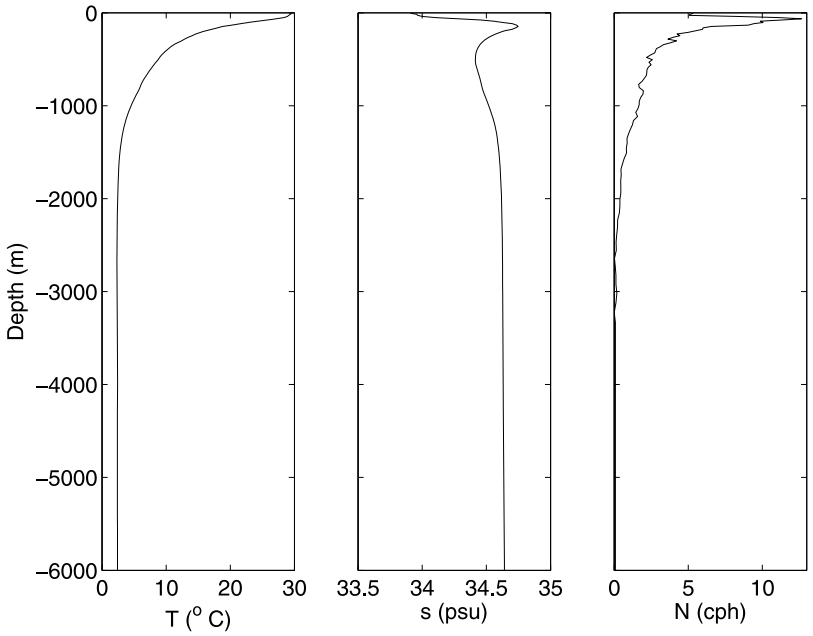

Figure 2. Observed profiles of temperature and salinity used to initialize the simulations, along with the computed buoyancy frequency. Data from *Ramp et al.* [2010].

layer is implemented in the model via a term on the right-hand side of the horizontal momentum equations of the form

$$S_j(x,y,z,t) = -\frac{u_j(x,y,z,t) - \overline{u}_j(x,y,t)}{\tau} s(r). \qquad (1)$$

Here, j = 1, 2 is the component of the horizontal velocity, $s(r) = \exp(-4r/L_s)$ causes the sponge layer to decay exponentially over the distance L_s = 50 km from the nearest open boundary which is a distance r from the point x, y, and τ = 1000 s is the damping time scale. In equation (1), the overline indicates a depth average, so that the sponge has little effect on the barotropic currents but effectively damps the baroclinic currents. The model is initialized with horizontally uniform stratification obtained from observations as shown in Figure 2, and the initial velocity field is quiescent. In what follows we refer to the n_{th}-mode eigenspeed of the waves that propagate in the absence of rotational and nonhydrostatic dispersion as $c_{n,0}$. A wave propagating with frequency ω is then corrected to account for rotational dispersion [see, e.g., *Helfrich*, 2007] with $c_{n,\omega} = c_{n,0}\,[1 - (f/\omega)^2]^{-1/2}$. The Coriolis parameter is constant in our domain and is given by its value at a latitude of 20.5°, $f = 5.1 \times 10^{-5}$ rad s^{-1}.

[11] The unstructured grid we employ is shown in Figure 3. This grid has a mean resolution of 1358 m, a mode of 687 m, a minimum resolution of 75 m, a maximum resolution of 4740 m, and a standard deviation of 710 m. In order to resolve the tidal-scale generation physics at the Luzon Strait and subsequent dynamics of interaction with the continental shelf, the grid resolution is roughly 1 km near the Dongsha Atoll and in the vicinity of the eastern ridge in the Luzon Strait (around the Batan and Babuyan Islands). The grid has a nominal resolution of 2 km in the main SCS basin and 4 km near the boundaries of the domain. In the vertical, 100 layers are used with a minimum resolution of 10 m near the surface and expanding to 203 m at the bottommost cell. In total, the three-dimensional domain is discretized with 11 million computational cells. The model thus requires roughly 4 GB of RAM.

[12] The horizontal grid resolution can be much smaller than the mean resolution of 1358 m in parts of the domain. Therefore, the time step size must be chosen to ensure stability associated with temporally resolving the first-mode baroclinic wave (since the barotropic mode is discretized implicitly) at the minimum grid spacing. The smallest horizontal grid spacing of $\Delta x_{\min}$ = 75 m occurs where the depth is 1000 m. At this depth, the linearized first-mode phase speed is $c_{1,K1}$ = 3.4 m s^{-1}. Here we use the diurnal frequency to ensure stability since it produces waves that are 20% faster than those with the semidiurnal frequency. Theoretically, the maximum time step size is then given by $\Delta t_{\max} = (\Delta x/c_{1,K1})_{\min} = 22$ s. In practice we find that stability is achieved with a Courant number of $C_{\max} = (c_{1,K1}\,\Delta t/\Delta x)_{\max} = 0.5$. Therefore, we use a time step size of $\Delta t = C_{\max}(\Delta x/c_{1,K1})_{\min}$ = 11 s, which requires 122 000 time steps to simulate the period encompassing 30 M_2 tidal cycles that begins on 17 June 2005. The horizontal diffusion coefficient is constant and given by ν_H = 1 m^2 s^{-1} and the vertical diffusion coefficient is constant and given by $\nu = 10^{-4}$ m^2 s^{-1}. These are minimum values set by stability requirements of central differencing for momentum advection, and so decreasing them requires more grid resolution. However, as discussed by *Jachec* [2007], increasing the diffusion coefficients by 1 order of magnitude affects short-wavelength features but the large-scale internal wave energetics remain largely unaffected. No turbulence model is employed and diffusion of scalars is ignored. We use 64 processors on the JVN LinuxNetworx 64EMT cluster at the Army Research Laboratory Major Shared Resource Center (ARL MSRC) in Aberdeen Proving Ground, MD.

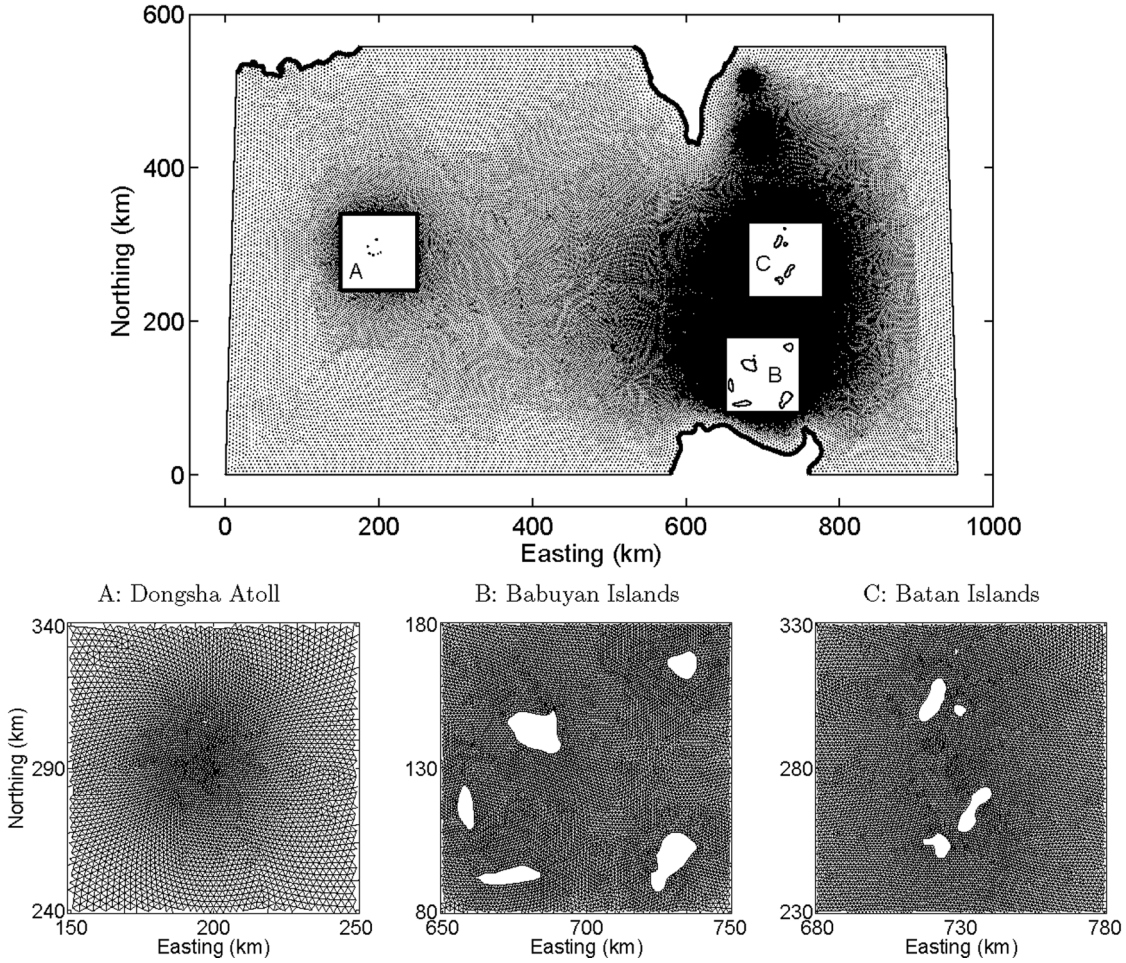

Figure 3. Unstructured grid of the domain used to simulate NLIW in the SCS. (top) Triangle vertices (i.e., no edges) shown for clarity, and (bottom) grids within the boxed regions are depicted.

The model runs twice as fast as real time, requiring 7 wall clock days, or 11 000 CPU hours, for the simulation results presented in this paper.

3. Model Validation

3.1. Comparison to Barotropic Tides at the Batan Islands

[13] Because internal waves are generated by the interaction of barotropic tidal currents with irregular topography, reproduction of the barotropic tidal currents in the Luzon Strait is essential to simulate the generation of internal waves in the SCS. Figure 4 shows the east-west barotropic velocities from field observations obtained at mooring L1 (see Figure 1) during the 2005 WISE/VANS field program [*Ramp et al.*, 2010]. The observed tidal currents at mooring L1 are characterized by a fortnightly cycle with strong spring-neap variability. During the simulation period the strongest currents are predominantly diurnal and occur around 23 June 2005. The weakest currents are predominantly semidiurnal and occur at the end of the month. The currents also exhibit an asymmetry in that there are stronger ebb tides toward the Pacific Ocean than flood tides toward the SCS.

[14] A comparison between predicted and observed tidal currents at mooring L1 is depicted in Figure 4. The observed currents were obtained by averaging the moored velocity data which extended over the range −450 to −380 m. Superimposed over this are the predicted barotropic currents (averaged over the entire depth) from SUNTANS and OTIS [*Egbert and Erofeeva*, 2002]. We also show SUNTANS predictions averaged over the same portion of the water column as the observations. The OTIS results underpredict the barotropic currents. This is expected due to the unresolved complex bathymetry in the OTIS model. The SUNTANS barotropic currents at mooring L1 are larger than the OTIS predictions because of the higher-resolution bathymetry employed in the SUNTANS model. However, the SUNTANS barotropic predictions are still smaller than the observations. To determine if the discrepancy between the predicted currents and the observations is due to baroclinicity at mooring L1, we average the SUNTANS predictions over the same range as the observations. The average over the limited portion of the water column produces peak ebb (positive) currents that are slightly stronger than the predicted barotropic currents, although they are still smaller than the observations. The strongest observed ebb tide is 1.5 m s^{-1}, while that computed by the SUNTANS

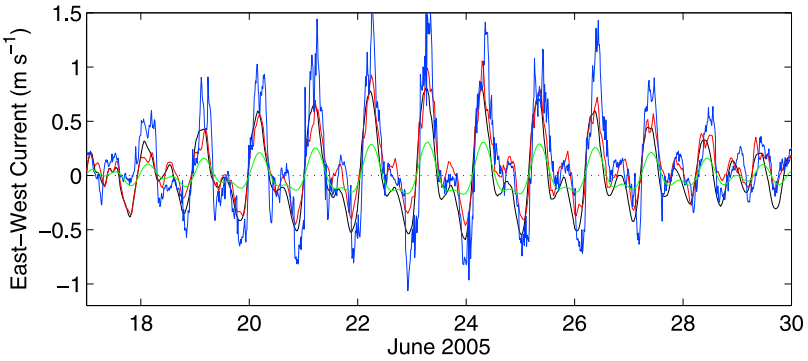

Figure 4. Comparison of east-west currents at mooring site L1 during the period 17–30 June 2005. Positive velocity indicates ebb tide toward the Pacific Ocean. The observations (blue [from *Ramp et al.*, 2010]) are obtained by averaging the currents from −450 to −380 m. For SUNTANS model results, the black line shows the barotropic velocity, while the red line shows the velocity averaged from −450 to −380 m. The green line shows the OTIS results. Model-data comparison of tidal constituents is shown in Table 1.

model is 1.1 m s^{-1} (averaged over the same portion of the water column). This mismatch is likely due to underresolved bathymetry in the model that does not reproduce the strength or the complexity of the currents around the mooring. A much larger discrepancy between the limited average and the full depth average occurs during the weaker ebb tide. During this period, although the barotropic currents remain negative (or small), the limited average produces weak positive tidal currents, and the model predicts these peaks very well. The large discrepancy between the limited depth average and the barotropic currents during weak ebb (by both the model and the observations) indicates that the flow is strongly baroclinic, since the bottom currents flow toward the Pacific Ocean while the net barotropic flow is into the SCS.

[15] Model-predicted tidal constituents of the velocity averaged over the depth range −450 to −380 m are compared to the observed constituents in Table 1. The mismatch in the peak currents in Figure 4 arises predominantly from an underprediction of the M_2-derived currents, since currents from the other constituents are predicted reasonably well. We attribute the mismatch between the predicted and observed inclinations to the complexity of the bathymetry around mooring L1 that is not resolved by the model (see Figure 9 of *Ramp et al.* [2010] for a detailed view of the bathymetry in the vicinity of mooring L1).

3.2. Comparison to Temperature Profiles

[16] To further validate the SUNTANS model, temperature profiles obtained from in situ measurements during the WISE/VANS program [*Ramp et al.*, 2010] are compared to SUNTANS simulation results. Figures 5 and 6 show the comparison at the B1 and S7 mooring sites (see Figure 1 for the locations). Figures 5 and 6 show that SUNTANS predicts the arrival times of the A and B waves reasonably well at both moorings B1 and S7. However, as shown in Figure 6, the stratification in the model is slightly overpredicted on the shelf (higher temperatures exist in the upper water column in the model). This may be due to an underprediction of vertical mixing in the model. A constant vertical eddy diffusivity is employed which does not account for vertical mixing due to large-amplitude internal waves or wind.

[17] Figure 7 compares the predicted to observed amplitude of the 15° isotherm at moorings B1 and S7. On average, the model underpredicts the amplitude of waves by 53% at mooring B1 and 27% at mooring S7. Waves with amplitudes that exceed 60 m at mooring B1 are the most underpredicted. Omitting these waves shows that, on average, the model underpredicts the amplitude of waves at B1 by 29%. Table 1 shows that the sum of the computed dominant semimajor axes for the barotropic tidal ellipses at location L1 is 24% smaller than what is observed. This may account for the amplitude error for the waves at B1 with amplitudes less than 60 m. For the waves exceeding 60 m in amplitude at mooring B1, the underprediction is magnified due to lack of model resolution that cannot capture the dispersion of the steep solitary-like waves as they propagate across the basin.

3.3. Comparison to Satellite Imagery

[18] Satellite imagery provides evidence for the existence of nonlinear internal waves in the SCS via their surface

Table 1. Harmonic Analysis of the Predicted and Observed Currents Averaged Over −450 to −380 m at Location L1 Using T_TIDE[a]

		Predicted			Observed		
Constituent	Period	Major	Minor	Inclination	Major	Minor	Inclination
K_1	23.93	0.25 ± 0.02	−0.04 ± 0.02	243 ± 4	0.27 ± 0.02	−0.05 ± 0.01	274 ± 2
M_2	12.42	0.21 ± 0.06	0.01 ± 0.04	264 ± 11	0.35 ± 0.01	0.01 ± 0.01	285 ± 2
O_1	25.82	0.20 ± 0.02	−0.05 ± 0.02	253 ± 5	0.27 ± 0.02	−0.06 ± 0.01	274 ± 2
S_2	12.00	0.06 ± 0.06	−0.02 ± 0.03	267 ± 37	0.14 ± 0.01	−0.00 ± 0.01	288 ± 4

[a]*Pawlowicz et al.* [2002]. The period is in h, while the semimajor and -minor axes are in m s^{-1} and the inclination is in degrees relative to true north. The errors represent the 95% confidence intervals.

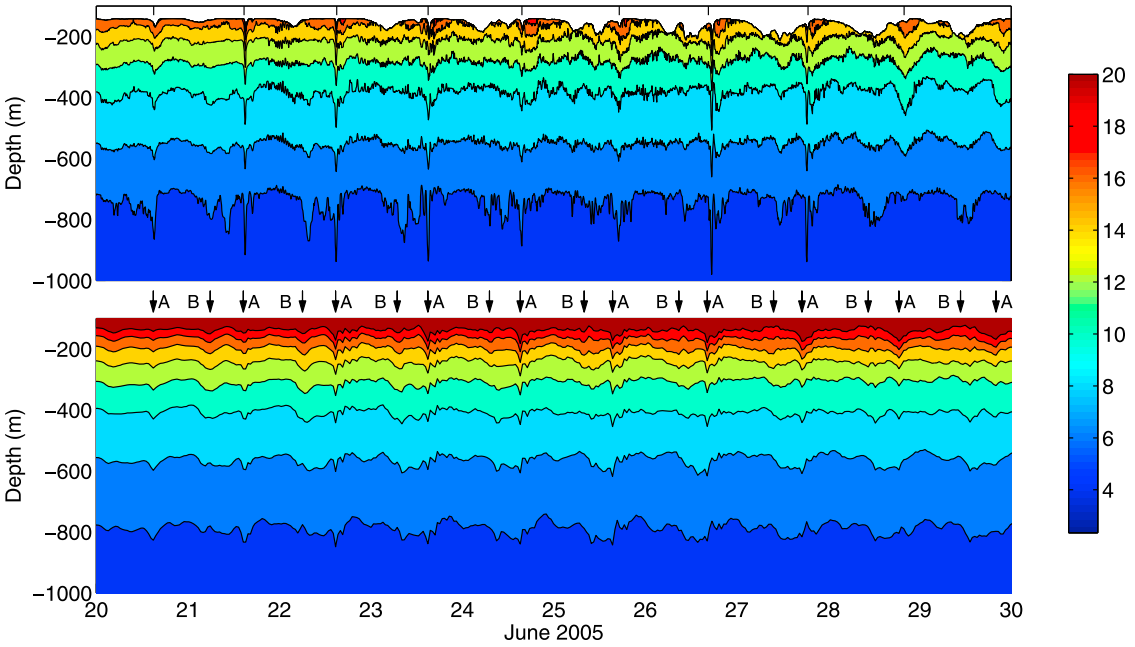

Figure 5. Model-data comparison of temperature profiles (in °C) at mooring site B1. (top) The temperature observed from the WISE field experiment in late June 2005 [*Ramp et al.*, 2010]. (bottom) The SUNTANS simulation results. Arrows indicate arrival times of A and B waves.

manifestations [*Hsu et al.*, 2000; *Hsu and Liu*, 2000; *Zhao et al.*, 2004; *Jackson*, 2009]. Figure 8a depicts a satellite image of the area around Dongsha Atoll on 26 April 1998 [*Hsu and Liu*, 2000]. Surface currents induced by internal waves create regions of convergence and divergence that modify the surface wave induced roughness and appear as bands in synthetic aperture radar (SAR) imagery. We compare our results to SAR imagery in three ways to demonstrate the degree to which different metrics obtained from the model match the SAR imagery. Because no SAR imagery was available for the simulation period covered in this paper (which was chosen to match the WISE/VANS

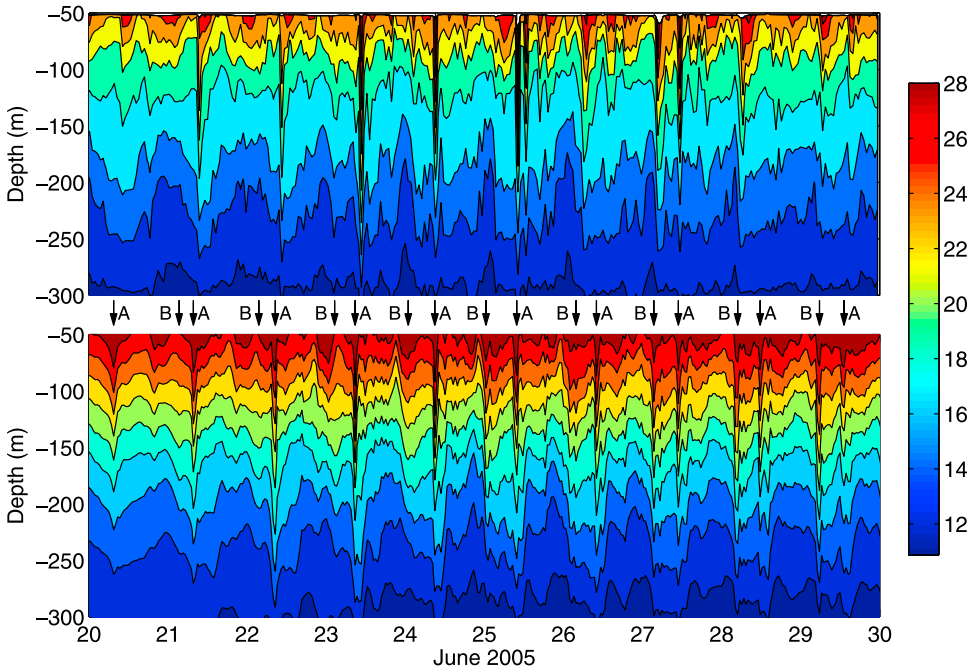

Figure 6. Model-data comparison of temperature profiles (in °C) at mooring site S7. (top) The temperature observed from the WISE field experiment (data shown at intervals of 50 min) in late June 2005 [*Ramp et al.*, 2010]. (bottom) The SUNTANS simulation results. Arrows indicate arrival times of A and B waves.

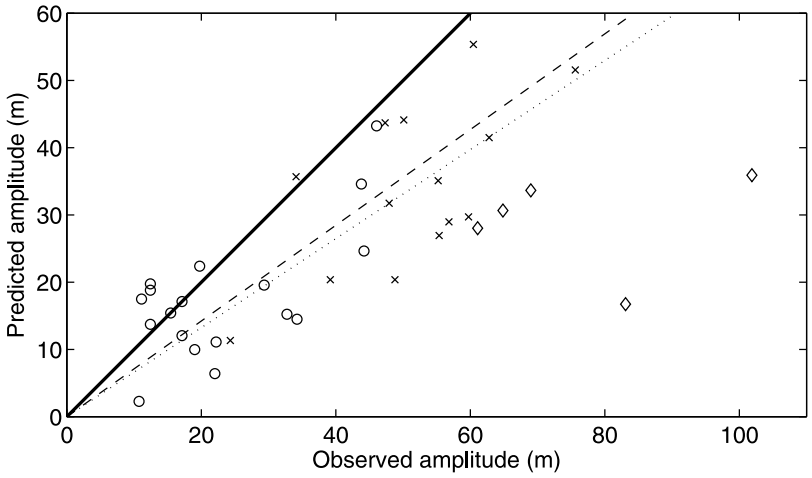

Figure 7. Model-data comparison of the amplitude of the 15° isotherm relative to its reference depth of 219 m for 22 waves at mooring B1 (circles and diamonds) and 14 waves at S7 (crosses). The solid line indicates an exact match. The simulated wave amplitudes at mooring B1 are 71% of what is observed (dashed line; inclusion of the five large-amplitude waves represented by the diamonds reduces this to 47%). The simulated wave amplitudes at mooring site S7 are 73% of what is observed (dotted line). Observations are from *Ramp et al.* [2010].

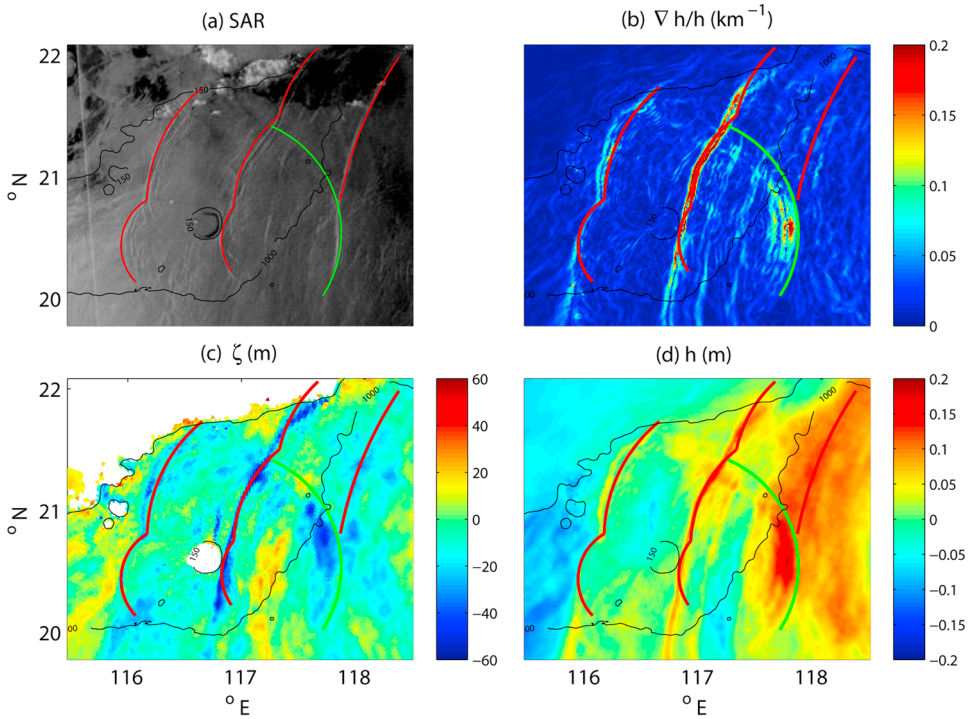

Figure 8. Model-data comparison of signatures induced by internal waves in the vicinity of Dongsha Atoll. (a) SAR image collected on 26 April 1998 from *Hsu and Liu* [2000]. (b)–(d) are model results obtained at 0623 on 2 July 2005. Figure 8b depicts the normalized magnitude of the gradient of the free surface elevation ($\nabla h/h$), Figure 8c depicts the displacement of the 20°C isotherm relative to the reference depth of 135 m, and Figure 8d depicts the free surface elevation relative to the sea surface height on the easternmost boundary of Dongsha Atoll (−0.2 m). The red arcs correspond to westward propagating waves visible in the SAR imagery, while the green arc corresponds to a reflected eastward propagating wave. Contours are also shown at 1000 and 150 m depth. These results are for the white dotted box depicted in Figure 1.

period of *Ramp et al.* [2010]), we choose model results from 2 July 2005 as these appear to match the SAR imagery most closely. The normalized magnitude of the simulated free surface gradient, $|\nabla h|/h$, is depicted in Figure 8b. Figure 8c depicts the displacement of the 20°C isotherm. Figure 8d depicts the free surface displacement, h, relative to the free surface displacement at Dongsha Atoll where the low tide incurs a free surface displacement of −0.2 m relative to mean sea level. All plots show the same qualitative behavior of the interaction of internal waves with the Dongsha Atoll. Because the depth is greater in the southern part of the image, the waves refract as the southernmost extent of the wavefronts propagates to the west faster. Nonlinear steepening in the shallow waters on the shelf causes the wavefronts to compress. The wavelength is therefore shorter for the wavefronts on the shelf than it is for the wavefronts in the deeper waters to the south. Upon encountering the Atoll, the waves diffract as they propagate around it, creating wavefronts that interact to its west. *Hsu and Liu* [2000] noted that a wave reflects off of Dongsha Atoll and propagates to the east, as indicated by the green arc in Figure 8. This wave is also captured by the model. Among the three plots of model results, the normalized magnitude of the free surface gradient in Figure 8b appears to match the SAR imagery most closely in a qualitative sense. This occurs because the SAR imagery is also an indicator of the surface divergence. The surface divergence, or velocity gradient induced by the internal waves, is in phase with the free surface gradient. We found that the horizontal velocity divergence at the surface (not shown) did not produce as favorable a match as the gradient of the free surface. The free surface displacement in Figure 8d closely follows the isotherm displacement in Figure 8c, suggesting that free surface waves of elevation are good indicators of the internal waves of depression. The linear relationship between the free surface and the interface deflection in an equivalent two-layer flow with a density difference of $\Delta\rho$ between the two layers is given by $\Delta h \approx -\Delta\rho/\rho_0\Delta\zeta$. From Figures 8c and 8d, the internal wave that abuts Dongsha Atoll has $\Delta h = +0.15$ m and $\Delta\zeta = -60$ m, implying $\Delta\rho/\rho_0 = 0.0025$, or a temperature difference of $O(10)$°C (assuming a thermal expansion coefficient of $\alpha = 2.5 \times 10^{-4}\ K^{-1}$). This is consistent with the observed thermal stratification depicted in Figure 2. The similarity between the observations and the model results demonstrates the ability of the SUNTANS model to correctly simulate the nonlinear behavior of internal waves as they shoal on the continental shelf and interact with the Atoll.

4. Internal Wave Dynamics

4.1. Wave Propagation and Evolution

[19] It is widely recognized that the nonlinear internal waves observed in the SCS originate within the Luzon Strait, where the bathymetry consists of two prominent ridges located roughly at 120.5°E and 122°E, as depicted in Figure 1. Figure 9 depicts the evolution of a set of waves at intervals of one half of one M_2 tidal cycle beginning at 0412 on 22 June 2005 and ending at 1205 on 24 June 2005. Waves are generated in the Luzon Straight and propagate westward and appear as dark bands in the surface color map of the isotherm depressions. The bands become darker and narrower as the waves steepen. Wavefronts propagate both to the east and west of the ridges because our model does not account for asymmetries resulting from the Kuroshio Current, as does that of *Chapman et al.* [2004]. However, eastward propagating waves are damped by the sponge layer on the eastern boundary and therefore do not have time to steepen into trains of solitary-like waves. The wavefronts that propagate to the west away from the Luzon Strait are not visible eastward of roughly 120.5°E. This is consistent with satellite imagery [e.g., *Liu and Hsu*, 2004; *Jackson*, 2009].

[20] The observations of *Ramp et al.* [2010] and *Alford et al.* [2010] show that two distinct types of waves propagate across the SCS basin, namely A and B waves. A waves appear at mooring S7 roughly at the same time every day, while B waves appear at mooring S7 roughly 1 h later each day. The A waves are stronger and appear as trains of solitary-like waves, while the B waves are weaker and appear as single wave peaks at mooring B1. Our results also produce two distinct waves. The B waves appear to the west of the A waves in Figure 9.

[21] The model produces internal wavefronts that form from the superposition of numerous internal wave sources. Superposition of numerous sources along a ridge, for example, form a line source that creates interference patterns in which the crest lines are strongest in amplitude along fronts that are parallel to the line source. This is similar to the interference patterns produced by the M_2 internal tide at the Hawaiian Ridge [*Rainville et al.*, 2010]. These interference patterns lead to the bands of internal wave tracks (rather than circular arcs) that propagate throughout the oceans as demonstrated by *Simmons et al.* [2004]. For linear waves, the interference patterns emanating from line sources remain relatively intact and can be traced back to their originating ridge. However, nonlinear effects can alter the interference patterns and produce circular wavefronts that radiate away from an apparent source that may not necessarily coincide with a particular bathymetric generation site. As we will show, the apparent generation sites are confined to a particular heading relative to actual internal wave bathymetric sources.

[22] As depicted in Figure 9c, waves A2 and B2 appear to form from two predominant sources that form two circular wavefronts. The southern front propagates northwest along Transect A. The northern front propagates along a more westerly heading parallel to Transect B. After propagating across the basin (see Figure 9f), waves A2 and B2 appear to have merged into more linear fronts. However, the merged A2 front propagates along Transect A while the merged B2 front propagates in a more westerly heading along Transect B. The propagation paths of the waves is consistent with the observations of *Ramp et al.* [2010] which show that the signatures of A waves are more nonlinear than those of B waves at mooring B1. At mooring B1, the A waves appear as distinct rank-ordered solitary-like wave groups while the B waves appear as single, weaker-amplitude waves. This behavior at mooring B1 can be seen in Figure 9f, which shows that the largest-amplitude portion of wave B2 has propagated to the south of mooring B1, while the largest-amplitude portion of wave A2 is on a path that will traverse the mooring. Because the location of peak amplitude of the A wavefronts is centered closer to mooring B1, nonlinear

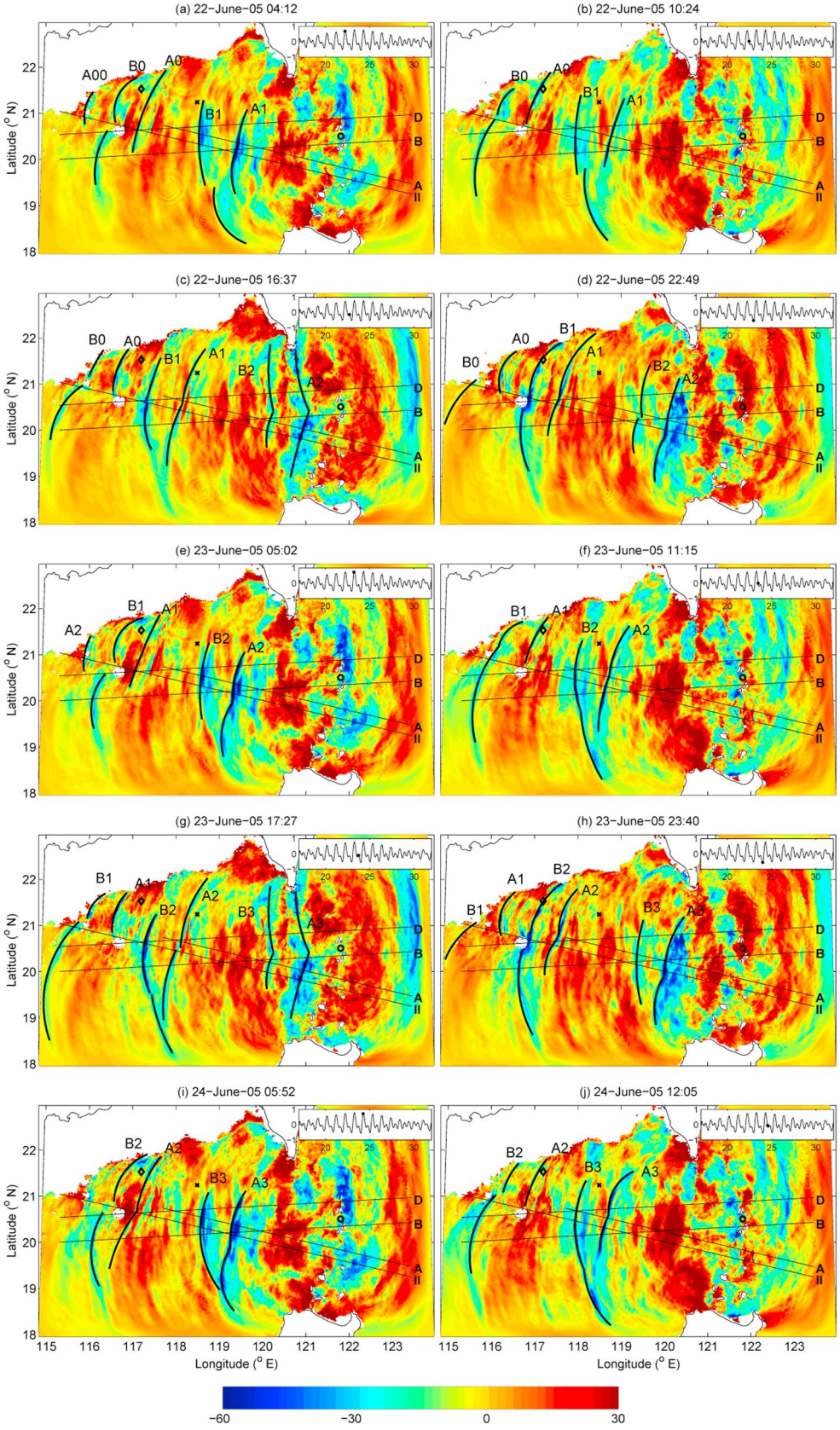
(a) 22−June−05 04:12
(b) 22−June−05 10:24
(c) 22−June−05 16:37
(d) 22−June−05 22:49
(e) 23−June−05 05:02
(f) 23−June−05 11:15
(g) 23−June−05 17:27
(h) 23−June−05 23:40
(i) 24−June−05 05:52
(j) 24−June−05 12:05
Latitude (° N)
Longitude (° E)
A00
A0
B0
A1
B1
A2
B2
A3
B3
D
B
A
II
−60
−30
0
30

Figure 9

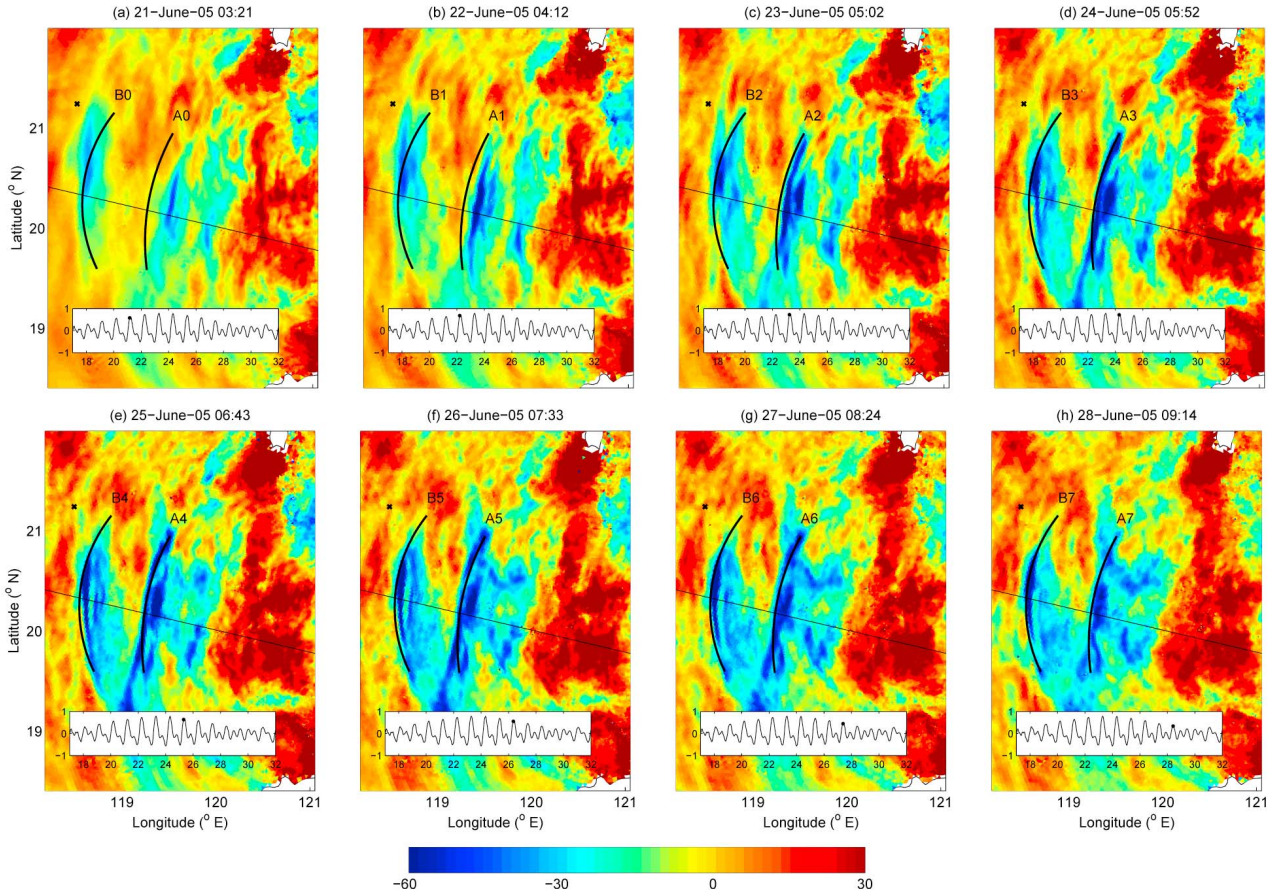

Figure 10. Elevation of the 20° isotherm relative to its depth at rest of 135 m at increments of two M_2 tidal cycles (24.82 h). The dark arcs correspond to the approximate locations of waves A6 and B6 on 28 June (Figure 10h) to show how the A waves migrate westward every two M_2 cycles, while the B waves appear roughly at the same location. The diagonal line indicates Transect II (see Figure 1) and the location of mooring B1 is indicated by the black cross. The inset plot shows the east-west barotropic tidal currents at mooring L1 (in m s^{-1}). The boundary of this region in the model domain is indicated by the solid white box in Figure 1.

effects lead to clear trains of waves in the time series as the A waves pass over the mooring. The B waves at this location do not appear as trains but instead appear as single peaks. Nonlinear effects for the B waves are stronger further to the south where the B waves form stronger wave trains as shown for wave B3 in Figure 9i.

[23] Although the A waves are generally larger to the north while the B waves are larger to the south in the western SCS basin, both waves disperse into trains of solitary-like waves as they encounter the shallow bathymetry of the continental shelf. The orientation of the shelf leads to refraction that steers the waves in a northwesterly heading. Because the shelf is shallower to the north of Dongsha Atoll, the wavefronts to the north steepen and disperse into more waves than those to the south. This behavior is also exhibited in the SAR imagery (Figure 8). The waves to the north diffract around Dongsha Atoll and interact with the waves to the south which also diffract around the Atoll, creating a complex wave-wave interaction pattern to the west of the Atoll. This behavior is consistent with the SAR imagery and simulated in detail under idealized settings by *Lynett and Liu* [2002].

[24] To determine the timing of the wavefronts, Figure 10 depicts the deflection of the 20° isotherm relative to its undisturbed depth of 135 m, plotted every two M_2 tidal cycles, beginning on 21 June 2005. Superimposed over the isotherms are the approximate circular wavefronts (indicated by the thick black lines) that correspond to waves A7 and

Figure 9. Elevation of the 20° isotherm (in m) relative to its depth at rest of 135 m at intervals of one half of one M_2 tidal cycle (6.21 h) over five M_2 tidal cycles. Approximate locations of five sets of A and B waves (numbered 00, 0, 1, 2, and 3) are indicated by the dark arcs. Transects A, B, D, and II (see Figure 1) are shown along with the location of moorings L1 (open circle), B1 (cross), and S7 (diamond) for reference. The inset plot shows the east-west barotropic tidal currents at mooring L1 (in m s^{-1}).

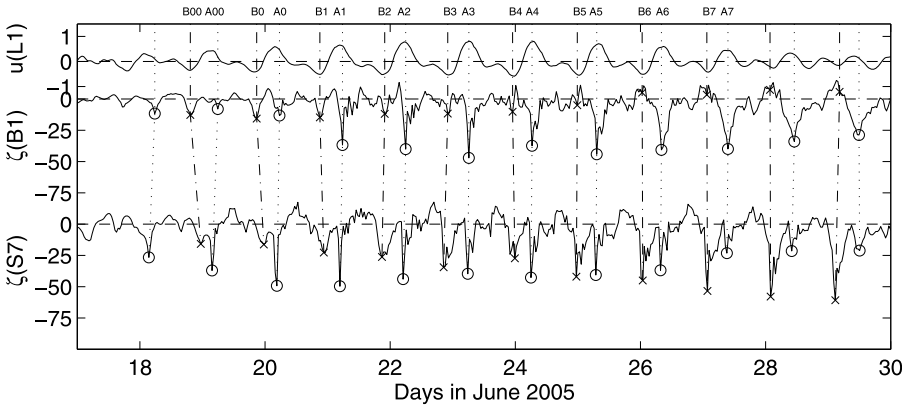

Figure 11. Time history of the displacement of the 20° isotherm (in m) at locations B1 and S7 due to waves 00–7 (circles, A waves; crosses, B waves), along with the east-west barotropic velocity at location L1 (u(L_1), in m s^{-1}). The signal at location B1 has been shifted backward in time by 33 h, while that at S7 has been shifted backward in time by 52 h. Plan views of the evolution of waves 00, 0, 1, 2, and 3 are shown in Figure 9.

B7 at 0914 on 28 June 2005 (Figure 10h). As the strength of the barotropic tides varies over the spring-neap cycle, so does the amplitude of the waves. Although the peaks in the B waves in Figure 10 appear at roughly the same location, the peaks in the A waves migrate westward every two M_2 tidal cycles. For example, the depression associated with wave A0 in Figure 10a is roughly 0.25° east of the most westerly location of the depression associated with wave A3 in Figure 10d. This westerly migration is consistent with the observations of *Ramp et al.* [2010], which show that A waves arrive at mooring B1 roughly at the same time every day, while the B waves arrive roughly 1 h later each day. The westward migration of A waves in our simulations is due to the behavior of the barotropic tides and depends weakly on amplitude dispersion. As will be discussed below, the amplitude of the waves is not large enough in the midbasin to induce significant amplitude dispersion.

[25] Figures 11 and 12 show time series of the isotherm depressions associated with A and B waves as they propagate past locations B1 and S7 along Transect I and past locations B2 and S8 along Transect II. Like the observations of *Ramp et al.* [2010], the waves closely follow the tidal signal in the Luzon Strait. Despite some variability over the spring-neap cycle, particularly during neap tides, the B waves consistently arrive earlier than the A waves by a time interval given by that between the peak westward and the peak eastward barotropic currents in the Luzon Strait. As shown in Figure 11, A waves are much larger than B waves at location B1. Here, A waves disperse into trains of solitary-like waves and B waves consist of single, small-amplitude peaks. As they shoal in shallower water, A and B waves are of equal amplitude and both disperse into trains of solitary-like waves at location S7. Despite the weakening of the tidal currents toward the end of the month, B waves continue to grow in amplitude at mooring S7 while A waves decay. Although the observations and the simulation results at mooring B1 indicate that A waves are larger in the deep basin, this only occurs because the propagation path of B waves is on a more westerly heading than A waves. At location B2, B waves are significantly larger than A waves,

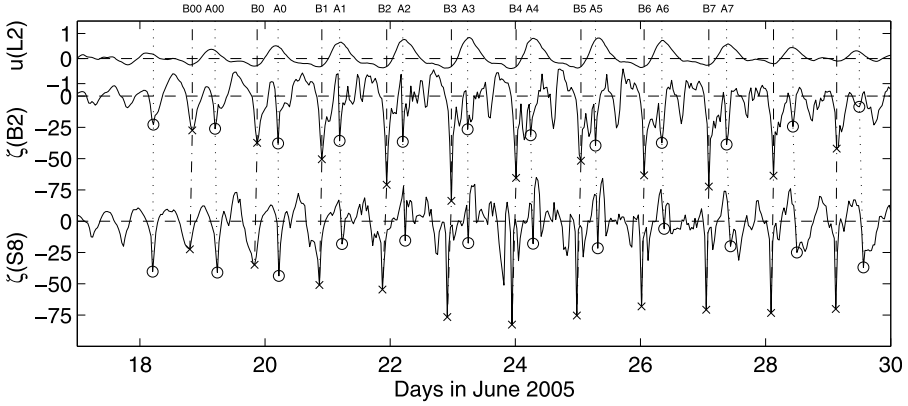

Figure 12. Time history of the displacement of the 20° isotherm (in m) at locations B2 and S8 due to waves 00–7 (circles, A waves; crosses, B waves), along with the east-west barotropic velocity at location L2 (u(L_2), in m s^{-1}). The signal at location B2 has been shifted backward in time by 31 h, while that at S8 has been shifted backward in time by 45 h. Plan views of the evolution of waves 00, 0, 1, 2, and 3 are shown in Figure 9.

Table 2. Travel Times and Average Speeds for Waves to Propagate Along Transects I and II[a]

	Travel Time (h)			
	L1-B1	L1-S7	L2-B2	L2-S8
Based on shift	33	52	31	45
From linear theory	31	47	31	44
	Average Speed (m s^{-1})			
	L1-B1	B1-S7	L2-B2	B2-S8
Based on shift	3.0	2.0	3.2	2.8
From linear theory	3.2	2.4	3.2	2.9

[a]The times are inferred from the shift required for the waves to line up with the tidal currents and from the time it takes for the first-mode wave corrected with the semidiurnal tidal frequency to propagate between the locations. The average speeds are computed from the travel times and distances between moorings.

as shown in Figure 12. On the shelf, B waves disperse so strongly that their trailing waves interact with and make it difficult to observe A waves at location S8.

[26] Following *Ramp et al.* [2010], the time series of the displacements in Figures 11 and 12 are shifted backward in time so that the A wave peaks are aligned with peak eastward tidal flow at the eastern ridge. Along Transect I, this requires a shift of 33 h for the time series at B1 and 52 h for that at S7, and shifts of 31 and 45 h for the time series at B2 and S8, respectively. These shifts correspond to the time it takes for the first-mode internal tide to propagate from the ridges that generate them to the locations of the time series. Using the linear first-mode wave speed corrected with the M_2 tidal frequency, the theoretical propagation times (as opposed to the times above which are those required to align the signals) are 31 (from L1 to B1), 47 (from L1 to S7), 31 (from L2 to B2), and 44 h (from L2 to S8). These are summarized in Table 2, which also shows the average speeds inferred from the shifts and propagation times. In general, the required shifts agree well with the predictions from theory along Transect II. However, the shifts along Transect I are longer and the inferred phase speeds are slower than those predicted from linear theory. Although the shift along Transect I is based on aligning A waves with peak eastward currents at L1, A waves are generated further to the south closer to L2 (discussed later), and hence the shift is longer than would be predicted by linear theory because mooring B1 is farther from L2 than from L1. The shift of 33 h for waves at B1 to align with currents at L1 is consistent with the observations of *Ramp et al.* [2010]. However, because the shift is based on aligning A waves, the lines connecting B wave peaks between moorings B1 and S7 in Figure 11 are not always vertical. The variability in the alignment may be due to modulation of the onshelf waves by locally generated internal tides [*Alford et al.*, 2010].

[27] More detail on the model-predicted phase speeds is obtained via computation of the speeds using the locations of waves A5 and B5 as they propagate along Transect II from 25 to 27 June (see Figure 14). As shown in Figure 13, the model-predicted phase speeds for both A and B waves are close to one another in the deep basin and closely follow the linear phase speed associated with the semidiurnal internal tide, which is denoted by $c_{1,M2}$. This implies that both waves are semidiurnal in character although the mechanism by which A waves are generated is strongly modified by the diurnal tides in the Luzon Strait. This semidiurnal behavior of the phase speeds is consistent with the observations of *Alford et al.* [2010]. However, their results showed a clear finite amplitude effect which led to 11% and 5% increases in the observed phase speeds of A and B waves, respectively, in the deep basin relative to $c_{1,M2}$. When the waves shoal, the observations of Alford et al. show that, despite being larger, B waves are slower than A waves due to modulation by the local internal tide. Our results show similar amplitude behavior in that the B waves grow larger than the A waves west of 119°, although the B waves are faster. Furthermore, the model computes A and B wave speeds that are slower than the linear phase speed. This may be due to modulation by the local internal tide as suggested by Alford et al., although the local internal tide can also accelerate the waves. Discrepancies between our results and those of Alford et al. may exist because their observations were not on the same line as Transect II. However, nonlinear effects are not correctly reproduced by the model because it underpredicts the internal wave amplitudes.

4.2. Correlation With Tidal Currents at the Eastern Ridge

[28] The distribution of waves in the SCS is a combination of first- and higher-mode waves that result from higher-mode generation due to barotropic flow over topography and scattering as the waves propagate westward into the SCS basin [*Johnston et al.*, 2003; *Peacock et al.*, 2009]. In section 4.4 we analyze the baroclinic currents and how they lead to the formation of the A and B waves. In this section we use the Hovmöller diagram, following *Alford et al.* [2010], to demonstrate the signatures of the first and higher modes that radiate away from the ridges. We also study correlation of the waves with the phase in the barotropic tide at the ridges. The Hovmöller diagram of the displacement of the 20° isotherm along Transect II is depicted in Figure 14. To highlight the time history of the westward propagating depression waves, regions with positive isotherm displacement are ignored and shown as white. The red crosses on the Hovmöller diagram correspond to the intersections of the B wave arcs with Transect II in Figure 10. The black open circles mark the intersections of the A wave arcs with Transect II. As discussed in section 4.1, because the time interval between these points is two M_2 tidal cycles, the location in space of the B waves remains unchanged, while that of the A waves moves westward.

[29] Superimposed over the Hovmöller diagram are the theoretical first- and second-mode internal wave characteristics that are obtained from a linearized normal mode analysis and corrected to include the effects of rotation at the M_2 tidal frequency. The theoretical first-mode characteristic curves were created via tracing both forward and backward in time from the points in time and space at which the simulated waves lined up with the vertical dashed line in the Hovmöller diagram at 118.6°E. This corresponds to location B2 on Transect II. The second-mode characteristic curves were then created by tracing them westward and forward in time starting from the point in time at which the first-mode A and B waves intersect the eastern ridge near 122°E. The

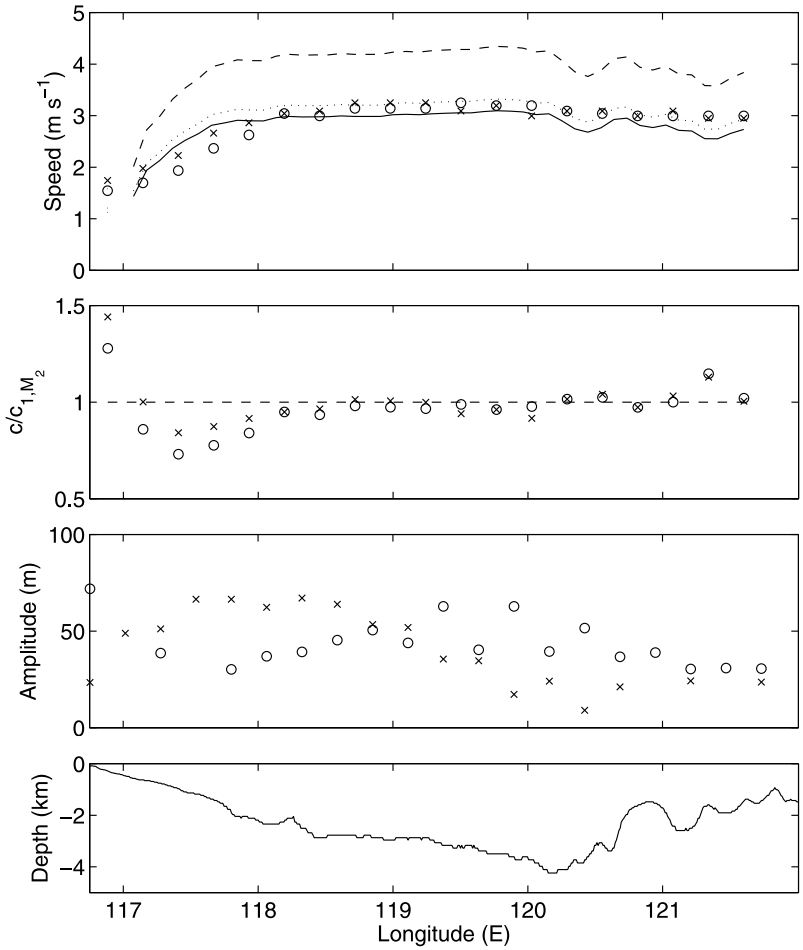

Figure 13. Simulated phase speeds and amplitudes for waves A5 (circles) and B5 (crosses) as they propagate along Transect II during 25–27 June 2005. The points that were used to compute the speeds are depicted in Figure 14. Linear phase speed without rotation ($c_{1,0}$), solid line; linear phase speeds corrected for the semidiurnal frequency ($c_{1,M2}$), dotted line; linear phase speeds corrected for the diurnal frequency ($c_{1,K1}$), dashed line.

results show good agreement between the actual and simulated characteristic tracks of the isotherm displacements, particularly for the first-mode waves. The agreement is very good east of 118.6°E, while west of 118.6°E the waves shoal and, due to modulation by the local internal tide as discussed in section 4.1, the speeds decrease below that predicted from linear theory. This is indicated by the deflection of the depressions above the linear characteristics. The speeds of the second-mode waves match very well with those predicted from linear theory. The slopes of the simulated and theoretical characteristic curves are in good agreement, at least east of 118.6°E. Although the theoretical mode 2 B wave characteristic curves line up consistently with the simulated results, the simulated mode 2 A waves line up well with the theoretical characteristic curves only toward the beginning of the simulation. As the simulation progresses, the simulated mode 2 A waves are shifted later in time than predicted by the theoretical characteristic curves. Because the mode 2 theoretical characteristics were assumed to originate at the same point in time and space as the mode 1 curves, this implies that the mode 2 B wave is consistently generated at the same phase in the tide as the mode 1 B wave. However, the mode 2 A waves appear to be generated later in time than the mode 1 A waves and this time delay increases during spring tides. This may be due to hydraulic effects on higher modes which may propagate more slowly than the peak barotropic currents.

[30] A zoomed-in view of the Hovmöller diagram in Figure 14 is depicted in Figure 15. Figure 15 presents a clearer picture of how the second-mode theoretical characteristics for the A waves consistently appear earlier than the simulated characteristics. Despite this disagreement, it is quite clear that the main features in the time series of the displacement of the 20° isotherm at a particular point in space will result from the passage of first- and second-mode A and B waves. As an example, Figure 15 (right) depicts time series of the displacement of the 20° isotherm along the vertical lines in the Hovmöller diagram. The isotherm displacement at the westernmost location (the solid line) shows three distinct features that occur periodically. The first feature is the largest and is a superposition of mode 2 A waves and mode 1 B waves (m2-A/m1-B), the second feature is the passage of a mode 1 A wave (m1-A), and the third is the passage of a mode 2 B wave (m2-B). The largest isothermal

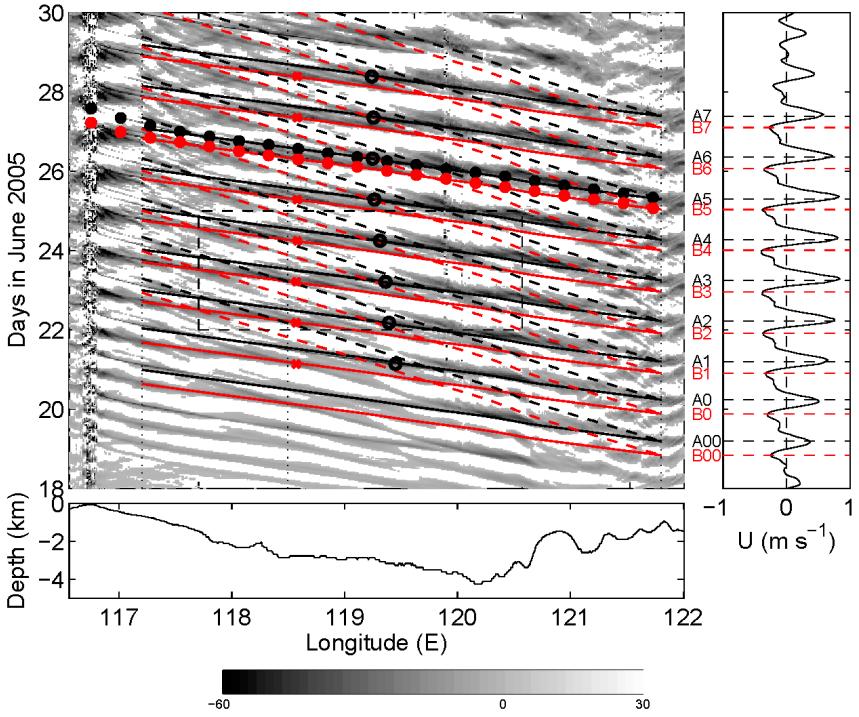

Figure 14. (left) Hovmöller diagram of the displacement (in m) of the 20° isotherm along Transect II. White regions indicate positive displacement to accentuate waves of depression. Solid black lines are the characteristics given by the speed of the linear semidiurnal internal tide ($c_{1,M2}$) following A waves. Solid red lines are those following B waves. The dashed lines follow the corresponding second-mode characteristics. (right) The barotropic currents at the eastern ridge (location L2), and the dashed lines indicate the times at which the A (black) and B (red) waves cross the eastern ridge. Plan views of the evolution of waves 00, 0, 1, 2, and 3 are shown in Figure 9. The intersections of waves 00–7 with Transect II in Figure 10 are indicated by the open circles (A waves) and red crosses (B waves). The data at the black filled circles (wave A5) and red filled circles (wave B5) are used to compute the results for Figure 13. A detailed view within the dashed rectangle is depicted in Figure 15. The three vertical dotted lines in the Hovmöller diagram indicate (from west to east) locations S8, B2, and L2.

displacement is due to the superposition of waves, but only at this location in space. Just 20 km to the east, as indicated by the dashed line time series in Figure 15 (right), the most dominant feature in the time series is the passage of a large mode 1 A wave. This is followed by the small mode 2 B wave and preceded by the m2-A/m1-B superposition of waves that is much smaller in amplitude than it is 20 km to the west. Although most of the energy is in the first mode, the spatiotemporal variability of the velocity and density fields results from superposition of first and higher modes. This may make it difficult to accurately assess phase speeds by following peaks in the isotherm depressions. As an example, in Figure 15 (right), the superposition of the m2-A/m1-B wave creates a peak in the depression that does not move in time when the observational location shifts to the west, but instead leads to a peak that appears to grow in amplitude without propagating. This is in contrast to the m1-A peaks in the western time series which are shifted later in time relative to the peaks in the eastern time series.

[31] The Hovmöller diagram in Figure 14 shows that the B wave characteristics consistently cross the easternmost ridge during peak westward flow in the tide. The A wave characteristics, on the other hand, consistently cross the ridge during or near peak eastward flow in the tide. This same result was found by *Ramp et al.* [2010] and *Alford et al.* [2010], although the correlation was not as clear due to the presence of low-frequency currents on top of which the internal waves propagate. It is also difficult to trace waves back to the generation sites with minimal observations through the complex internal wavefield in the Luzon Strait. The phase in the tide at which internal wave characteristics appear to cross the ridges where they originate is highly sensitive to the nonlinearity, topography, and modal structure of the waves. *Zhang* [2010] shows that westward propagating characteristics of linear internal tides in a two-layer stratification coincide with the ridges during slack water at the end of the ebb tide. Observations and the present model results contradict this finding due to the presence of more beamlike generation. However, the presence of nonlinearity can make the waves appear as if they are generated at the end of ebb tide like the linear two-layer model. For example, *Buijsman et al.* [2010b] show that the characteristics of leading solitons can appear to coincide with the end of the ebb tide. This occurs only if they propagate over enough time to allow characteristics of the depression waves to converge upon those of the elevation waves due to weakly nonlinear effects. This does not occur in the SCS because steepening is arrested and the char-

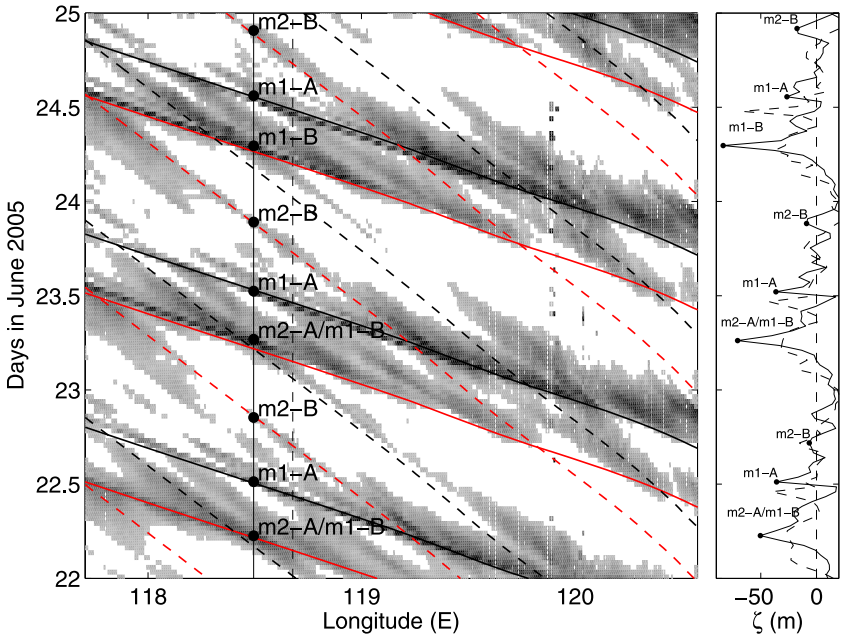

Figure 15. (left) Zoomed-in view of the boxed region in Figure 14. (right) The time series of the displacement of the 20° isotherms along the vertical lines at 118.6°E (solid line) and 118.7°E (dashed line). The corresponding waves that make up the signal in the westernmost time series (solid line) are indicated, namely modes 1 and 2 A waves (m1-A and m2-A) and modes 1 and 2 B waves (m1-B and m2-B).

acteristics do not converge upon one another as quickly. Instead, particularly for weak forcing, the peaks in the large-scale depression waves that result from the internal tides that propagate to the west coincide with peak westward currents. This is consistent with our results for B waves. Although also generated due to predominantly linear forcing, A waves do not follow the same phasing relationship. As discussed in section 4.4, we hypothesize that A waves coincide with peak eastward currents due to the predominance of beamlike generation over wider and deeper topography than that for the B waves. Multiple sources can also influence the phasing. This may be why A wave characteristics coincide near, but not exactly during, peak eastward tidal currents.

[32] While the mechanism determining the phase in the tide at which the wave characteristics cross the ridge is not clear, the phasing demonstrates the dependence of generation on nonlinear effects. One might expect the phase in the tide at which characteristics emerge from the ridge to vary with the spring-neap cycle if hydraulic effects are important, which in turn might imply the lee wave mechanism of *Maxworthy* [1979]. However, because the spatial distribution of the characteristic curves of the first-mode A and B waves is locked to the same phase in the tide regardless of its strength (i.e., throughout the spring-neap tidal cycle), the generation mechanism is predominantly linear and indicative of the generation of internal tides that radiate away and steepen into weakly nonlinear solitary-like waves. Because the characteristics in the present simulations are very close to linear, this implies further that the waves that radiate away are very weakly nonlinear. That is, the nonlinearity leads to steepening and dispersion into wave trains but it does not lead to pronounced curvature of the characteristics. Characteristic curvature due to nonlinear steepening would be apparent if the waves were allowed to propagate farther west without the effects of bathymetry. When allowed to propagate over many wavelengths, characteristic curvature is clearly shown in the simulations of *Buijsman et al.* [2010b]. Far from the generation site, those simulations show that characteristics of the depression waves travel faster and converge upon those of the more slowly propagating elevation waves.

4.3. Internal Wave Sources

[33] The character of internal wave generation is typically classified according to the excursion parameter $\epsilon = U_0 k_b/\omega$ and the critical slope parameter γ/s. Here, k_b^{-1} is the characteristic scale of the topography, U_0 is a scale for the barotropic currents, and ω is the characteristic frequency. The slope of the topography is γ and s is the slope of the internal wave rays. As described by *Garrett and Kunze* [2007], *Vlasenko et al.* [2005], and *Laurent and Garrett* [2002], internal tides dominate when the excursion parameter is small or when the topographic scale is long relative to the tidal excursion. When the excursion parameter is large the tidal excursion exceeds the topographic scale and lee waves can form. Small values of the tidal excursion parameter lead to the formation of beams which radiate away from near-critical regions. Subcritical slopes radiate predominantly low-mode energy. In the Luzon Strait, the topography is supercritical with respect to both the M_2 and K_1 internal tides, as indicated by the regions of criticality in Figure 16. The excursion parameter cannot be computed directly because it requires assumptions about the topographic scale. However, from the transects in Figures 18 and 19, one can deduce that the topographic scale for the ridges is O(100 km). An upper bound estimate of the tidal

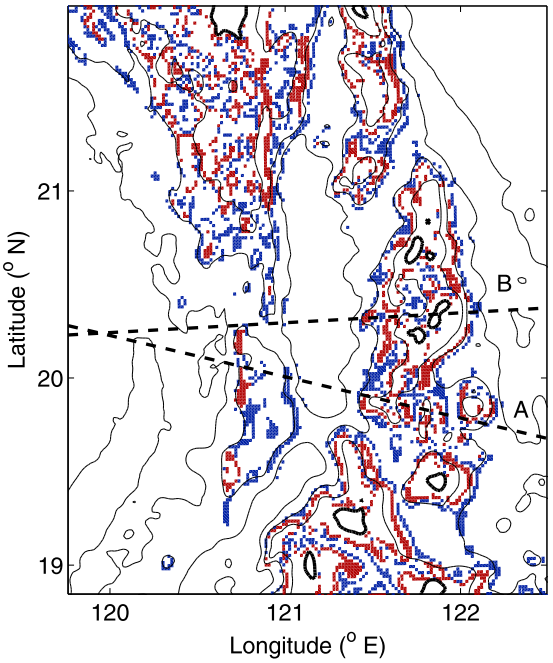

Figure 16. Contours of $0.75 \leq \gamma/s \leq 1.25$, where γ is the topographic slope and s is the slope of the internal wave ray for the K_1(blue) and M_2(red) tides. The black contours indicate bathymetry at intervals of 1000 m starting at 6000 m (the coastline is highlighted by the thick black contour). Transects A and B are indicated by the dashed lines.

excursion parameter given a maximum current speed of $U_0 = O(1\ \text{m s}^{-1})$ for the semidiurnal tide is then $\epsilon = 0.4$. Therefore, the lee wave effect on semidiurnal internal tides that radiate from the Luzon Strait is weak. The excursion parameter for the diurnal tide is twice as large at $\epsilon = 0.8$. Although this large value may imply lee wave effects, stronger generation associated with the diurnal tide is accompanied by weaker wave steepness owing to the longer wavelength. This reduces the nonlinear steepening of the diurnal internal tide which, when coupled with increased rotational dispersion, prevents the diurnal tide from forming solitary-like waves in the SCS [*Farmer et al.*, 2009]. It is important to note that there is small-scale topography in the Strait around islands that induce strong currents over short topographic scales, thereby implying much larger excursion parameters. For example the gap between Batan and Sabtang Islands is just 3–4 km wide, and tidal currents can be quite high in the presence of short topographic scales. While large-amplitude solitary waves are generated here [*Ebbesmeyer et al.*, 1991], we hypothesize that these waves comprise a small percentage of the large-amplitude waves that propagate into the SCS basin that arise from the predominantly linear internal tide.

[34] The low excursion parameter coupled with the presence of critical topography in the Luzon Strait lead to conditions suitable for the generation of internal wave beams at critical topography. Figure 17 shows the emergence of waves A2 and B2. The associated velocity profiles leading to the formation of these waves along the 12 transects depicted in Figure 17 are shown in Figures 18 and 19. As shown in Figure 16, both the eastern and western ridges contain slopes that are critical with respect to the semidiurnal and diurnal tides. Therefore, we overlay characteristics associated with both frequencies on all transects. The origins of the characteristics are chosen either at critical topography or, for cases in which the critical region is exceedingly shallow, the origins are chosen in a way that

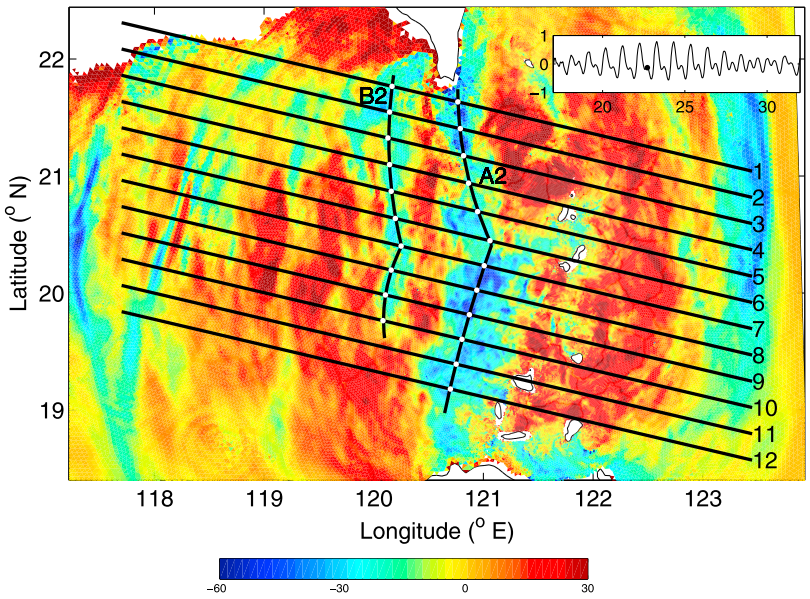

Figure 17. Detailed view of the elevation of the 20° isotherm (in m) relative to its depth at rest of 135 m at 1637 on 22 June 2005 (same as Figure 9c). Dark arcs indicate the approximate locations of emerging waves A2 and B2. The white circles indicate where these arcs intersect Transects 1–12. Profiles of the east-west velocity along these transects are shown in Figures 18 and 19. The inset plot shows the east-west barotropic tidal currents at mooring L1 (in m s^{-1}).

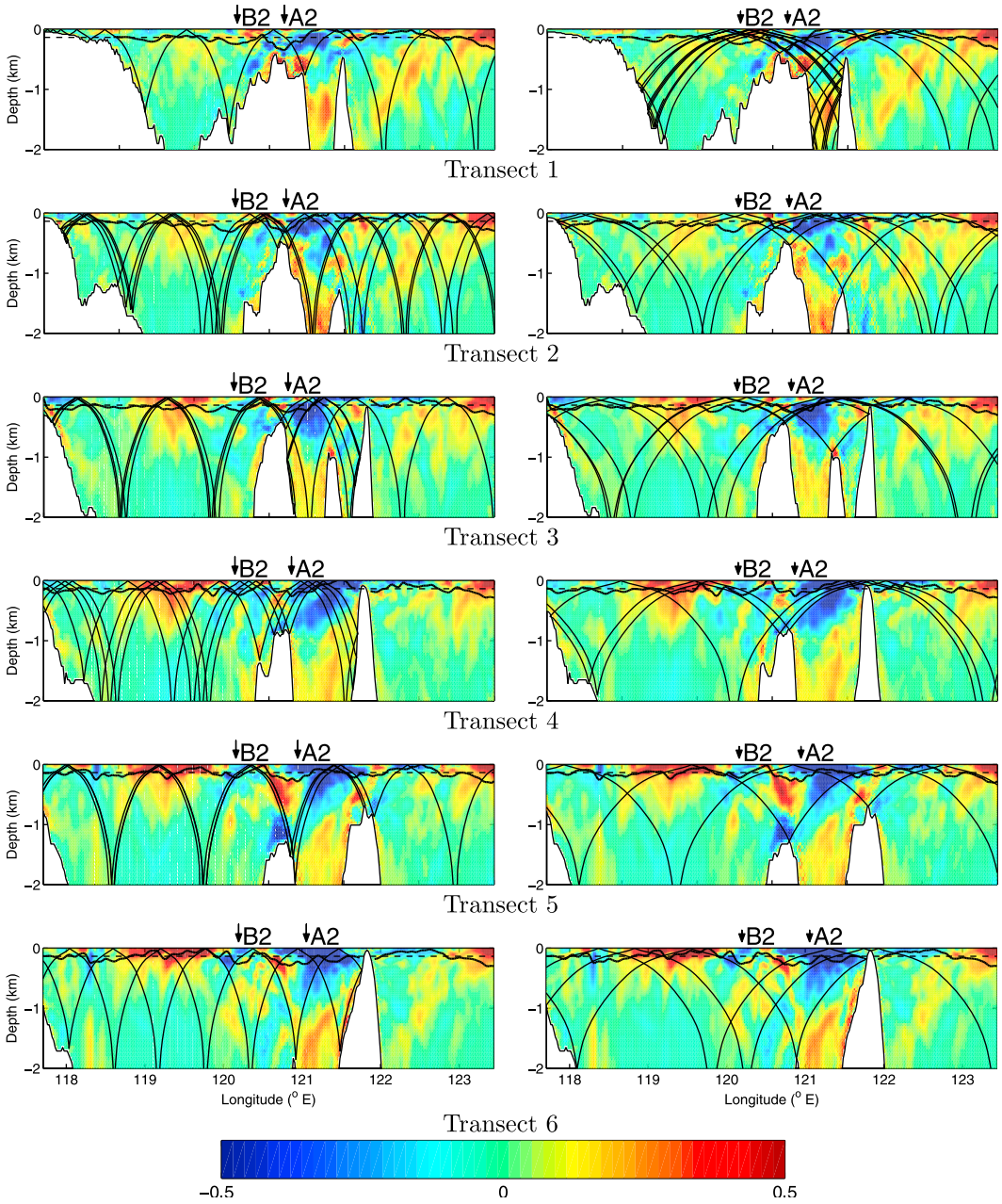

Figure 18. Profiles of east-west baroclinic velocity (in m s^{-1}) along Transects 1–6 depicted in Figure 17. (left) The M_2 internal wave characteristics and (right) K_1 internal wave characteristics are depicted. Locations of waves A2 and B2 are indicated by the arrows where their surface signatures are apparent in Figure 17.

allows the theoretical characteristics to most closely follow the baroclinic velocity field. The characteristics are computed using buoyancy-frequency profiles that are constant in time and in the horizontal. Therefore, some discrepancy may exist between the computed raypaths and the modeled velocity fields, particularly where the tidal currents are strong. In reality the internal wave raypaths in the Luzon Strait are also modulated by horizontal variability of the density field due to the Kuroshio intrusion. This effect will not be captured because our model is forced only by the barotropic tides.

[35] Both semidiurnal and diurnal frequencies are apparent in the baroclinic velocity fields in all transects in Figures 18 and 19. However, the western ridge appears to be the strongest generator of semidiurnal beams, particularly along Transects 5–9. The eastern ridge appears to be the strongest generator of diurnal beams, but further to the south along Transects 7–9. This may occur because the barotropic currents are more strongly diurnal to the south than they are to the north, as shown by the time series in Figure 20 and the tidal constituents in Table 3. The stronger diurnal behavior to the south is quantified by the form factor, which is the ratio of the magnitude of the diurnal (O_1 + K_1) to the

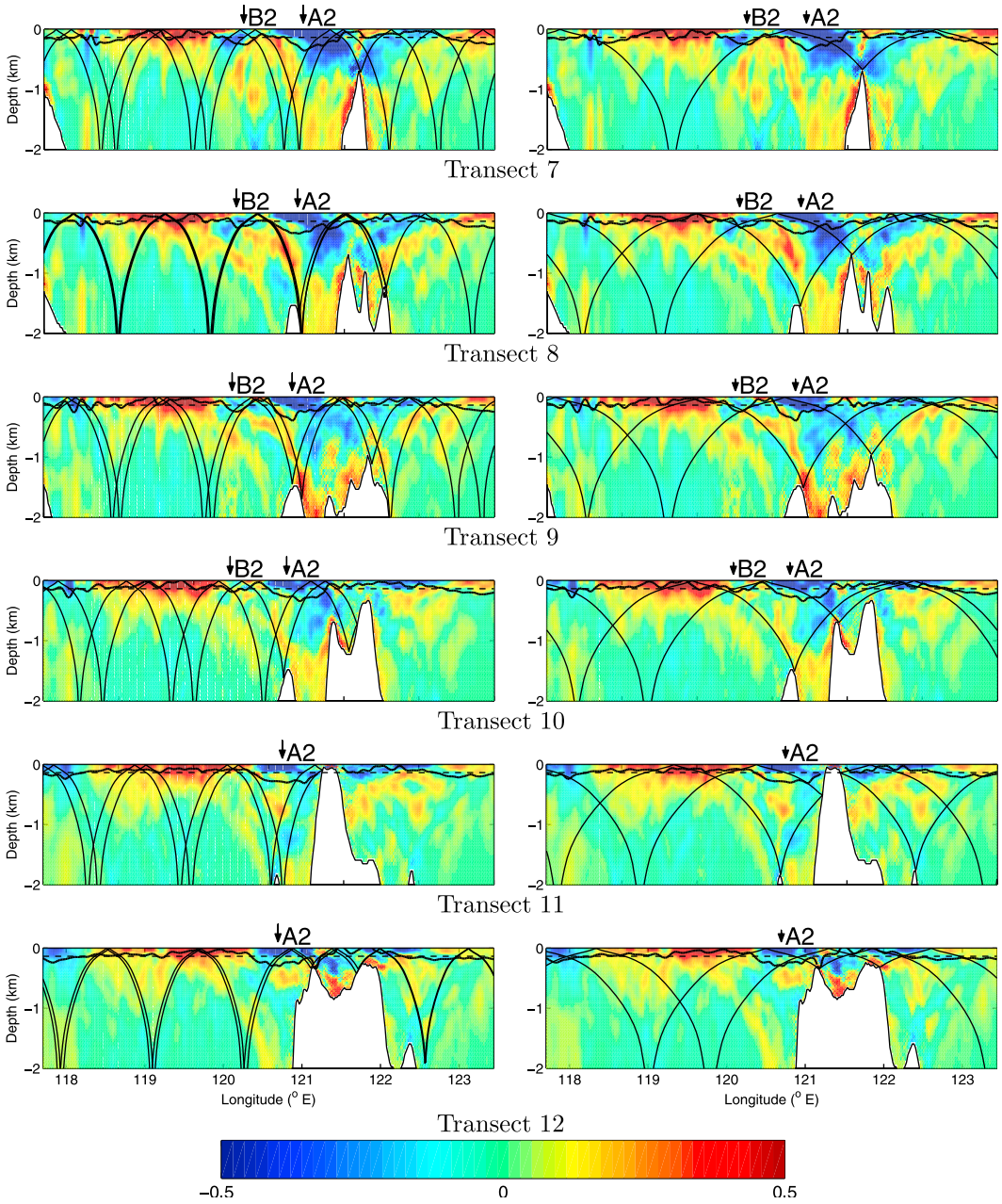

Figure 19. Profiles of east-west baroclinic velocity (in m s^{-1}) along Transects 7–12 depicted in Figure 17. (left) The M_2 internal wave characteristics and (right) K_1 internal wave characteristics are depicted. Locations of waves A2 and B2 are indicated by the arrows where their surface signatures are apparent in Figure 17.

semidiurnal (M_2 + S_2) constituents. Table 3 shows that to the north at L1 the form factor is 63% of that at L2.

[36] Although the velocity field is made up of the superposition of multiple-constituent internal tidal beams that originate from numerous regions in the Luzon Strait, there are specific regions at which the generation is strongest and form the primary generation locations for the A and B waves. To determine the approximate origins of these waves, the centers of the arcs corresponding to the A and B wavefronts in Figure 10 are shown in Figure 21. Transects A and B are determined via least squares fits to the corresponding arc centers. It is not clear exactly what causes the waves to originate at apparent sources that do not coincide with particular topographic generation sites. However, the apparent sources lie along paths that are consistent with observed and modeled internal wave propagation directions. Therefore, we hypothesize that the distance of the apparent source from the actual topographic source is set by weakly nonlinear processes related to the strength of generation which varies over the spring-neap tidal cycle. The heading of the apparent source is determined by the orientation of the topographic ridge that generates the waves. Weakly nonlinear processes act along this heading to produce the apparent generation sites.

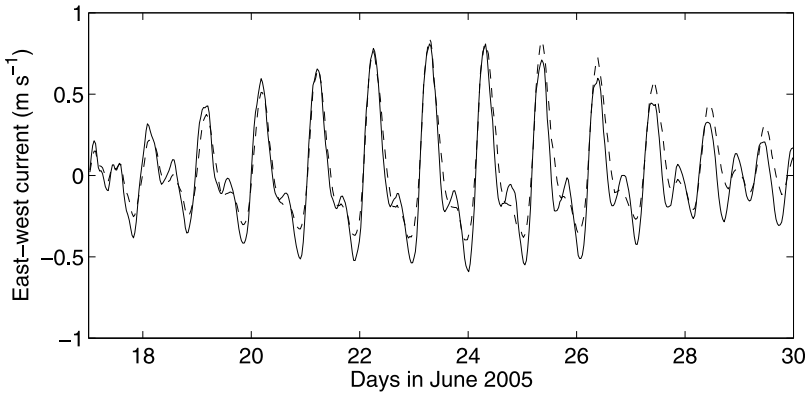

Figure 20. East-west barotropic currents at locations L1 (solid line) and L2 (dashed line), showing the stronger diurnal behavior of the currents at location L2. Tidal constituents are given in Table 3.

[37] The heading inferred from the apparent sources of the A wavefronts is consistent with the direction of propagation of 282° by *Ramp et al.* [2004]. The heading is also within the uncertainty bounds of the inclination of the semimajor axes of the K_1, O_1, and M_2 barotropic tidal ellipses at location L2 as tabulated in Table 3 and shown in detail in Figure 21. The inferred propagation path for the B waves is along a more westerly heading of 267° which is also within the uncertainty bounds of the inclination of the semimajor axes of the K_1, M_2, and O_1 barotropic tidal ellipses at location L1. It is possible to produce angle histograms to highlight the predominant direction of propagation of the waves as was done by *Ramp et al.* [2004]. These would produce A wave peaks near 282° and B wave peaks near 267°, and variability would arise due to topographic diffraction. Other peaks would appear due to reflection and local generation. For example *Ramp et al.* [2004] show that a peak in the angle histogram at mooring S7 arises due to reflected waves from Dongsha Atoll. Because of the sensitivity to location, we avoid analysis of the angle histograms. Instead we assume that the correlation between the inferred direction by the arc centers and the semimajor axes of the tidal constituents at the ridges provides convincing evidence for the wave propagation paths.

[38] Based on the inferred directions from the arc centers, it is likely that the strongest A wave signatures are generated due to cross-isobath flow over the eastern ridge to the south of Batan Islands, which we refer to as the A ridge in Figure 21. The strongest B waves are generated due to cross-isobath flow over the eastern ridge to the north, which we refer to as the B ridge. The A wave crests then propagate in a direction parallel to Transect A, which is perpendicular to the A ridge, and the B wave crests propagate in a direction parallel to Transect B, which is perpendicular to the B ridge. The generation mechanism is similar along both of these ridges, and in fact A and B wave generation occurs throughout the Strait to varying degrees (see Figure 22). However, the appearance of arcs with centers that consistently lie along Transects A and B indicates that the strongest A wave source lies along Transect A, while the strongest B wave source lies along Transect B.

4.4. Generation Mechanisms

[39] The surface plots in Figures 9 and 17 indicate that A and B waves are generated over the entire north-south extent of the Luzon Strait. Profiles of the evolution of both waves are depicted in Figure 22. We analyze the profiles along Transect D in Figure 22 because it does not intersect the Batan Islands and provides a more representative view of the large-scale behavior of waves normal to the B ridge. In Figures 9 and 17 the locations of A and B waves are based on the maximum depression of the 20° isopycnal. However, as shown in the Hovmöller diagram in Figures 14 and 15, superposition of different modes can make wave tracking based on the isopycnal depressions difficult. Furthermore, the location of the waves is unclear near the ridges before the waves have time to steepen into clear depression waves. Therefore, in Figure 22 the locations of the A and B waves are inferred by tracing the characteristics backward in time, beginning from points in time when obvious depression waves exist. Waves are traced backward in time in these profiles until the characteristics line up with the ridges.

Table 3. Harmonic Analysis of the Predicted Barotropic Currents at Locations L1 and L2 Using T_TIDE[a]

		L1			L2		
Constituent	Period	Major	Minor	Inclination	Major	Minor	Inclination
K_1	23.93	0.29 ± 0.02	−0.03 ± 0.01	257 ± 2	0.29 ± 0.02	−0.07 ± 0.01	284 ± 3
M_2	12.42	0.25 ± 0.03	−0.01 ± 0.02	266 ± 5	0.17 ± 0.02	−0.02 ± 0.01	281 ± 2
O_1	25.82	0.21 ± 0.02	−0.04 ± 0.01	256 ± 3	0.24 ± 0.02	−0.05 ± 0.01	282 ± 4
S_2	12.00	0.05 ± 0.03	−0.01 ± 0.02	91 ± 23	0.04 ± 0.03	0.00 ± 0.00	270 ± 7
M_4	6.21	0.01 ± 0.00	−0.01 ± 0.01	90 ± 17	0.02 ± 0.01	0.00 ± 0.00	332 ± 24
Form factor		1.65 ± 16			2.64 ± 16		

[a] *Pawlowicz et al.* [2002]. The period is in h, while the semimajor and -minor axes are in m s^{-1} and the inclination is in degrees relative to true north. The errors represent the 95% confidence intervals. Note that these results differ from those in Table 1, which are averaged over a limited portion of the water column at location L1.

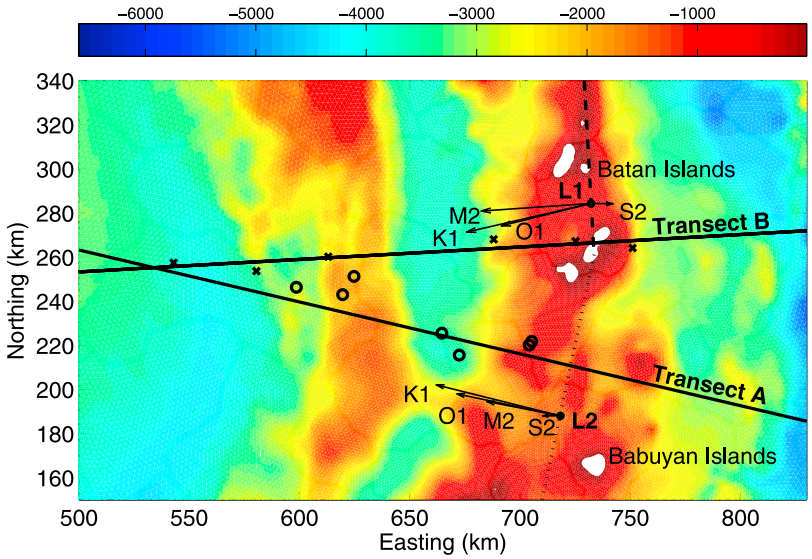

Figure 21. Zoomed-in view of the bathymetry (in m) region in the white dashed box in Figure 1, showing the centers of the arcs that are aligned with the wavefronts depicted in Figure 10 (circles, A waves; crosses, B waves). The arrows indicate the direction and relative magnitude of the semimajor axes of the barotropic tidal current ellipses (for values see Table 3). The dotted line is the A ridge, while the dashed line is the B ridge. All arrows over L1 are parallel to Transect B to within the uncertainties given in Table 3.

Waves that are indicated in Figure 22 may not be indicated in the surface plots in Figure 9 because it is not straightforward to trace wave characteristics backward in time in two-dimensional plan view (x-y) in the presence of numerous sources. Waves A3 and B3 are depicted from the time they are generated (A3 emerges in Figure 22d and B3 emerges in Figure 22a) to the time they propagate in the deep basin as solitary-like waves. In the deep basin, wave A3 is larger than wave B3 along Transect A and wave B3 is larger than wave A3 along Transect D.

[40] The results in Figure 22 show that, along both Transects A and D, the A waves can be traced back to peak eastward barotropic flow at the eastern ridge (e.g., wave A3 in Figure 22d) while the B waves can be traced back to peak westward barotropic flow (e.g., wave B3 in Figure 22a). The emergence of A waves is more clearly visible in the plots and can be seen by the near-surface westward baroclinic velocity near the ridges during peak eastward barotropic flow, particularly along Transect A in Figure 22d. When wave A3 emerges over the eastern ridge, the surface westward baroclinic currents arise from the upward energy propagation along the M_2 internal tidal ray that originates on the eastern flank of the eastern ridge. The newly formed A wave propagates to the west which is consistent with phase propagation that is down and to the west in the presence of upward and westward energy propagation. Westward baroclinic currents are visible in the upper water column following wave A3 in both Transects A and D in Figures 22d–22g. This is not the case for B waves, which are not as clearly visible until after emerging from the dual-ridge system (Transect A in Figure 22f and Transect D in Figure 22e).

[41] *Buijsman et al.* [2010a] and *Farmer et al.* [2009] show that A and B waves form as a result of generation arising from the superposition of the diurnal and semidiurnal barotropic currents. Formation of both wave types does not require two ridges nor does it require continuous stratification (*Farmer et al.* [2009] used a two-layer model). However, there are differences in the topography and tidal constituents that explain the differences in the strengths of the A and B waves along Transects A and D. *Buijsman et al.* [2010a] showed that the presence of the western ridge leads to resonance with the M_2 internal tide and amplification of the B waves because the western ridge is located a distance of roughly one M_2 internal tidal wavelength west of the eastern ridge. This can be seen in Figures 22d–22f along both Transects. The M_2 beam emanating from the eastern flank of the western ridge produces westward currents in the upper part of the water column that amplify wave B3 as it propagates. Because the B ridge has a stronger M_2 barotropic component (see Table 3) and the western ridge is more prominent to the north, stronger M_2 internal tidal beams emanate from the western ridge (e.g., Transects 5–9 in Figures 18 and 19). This provides stronger resonant conditions normal to the B ridge and produce larger-amplitude B waves along Transect D. Although western ridge M_2 resonance exists normal to the A ridge, K_1 internal tidal beams play a more important role there. As shown along Transect A in Figures 22f–22h, wave A3 is amplified by the westward currents produced by the K_1 ray emanating from the eastern flank of the eastern ridge. Westward currents from the M_2 internal tidal ray on the western ridge may also amplify the A wave, as shown in Figure 22h. This diurnal-semidiurnal superposition of internal wave rays is accentuated normal to the A ridge due to strong diurnal tides (see Table 3). As shown for Transects 7–9 in Figure 19, the deeper A ridge enables stronger westward transmission of diurnal beams.

4.5. A Simple Model for the Internal Wave Amplitude

[42] We can approximate the amplitude of the internal waves that propagate across the SCS basin using a simple

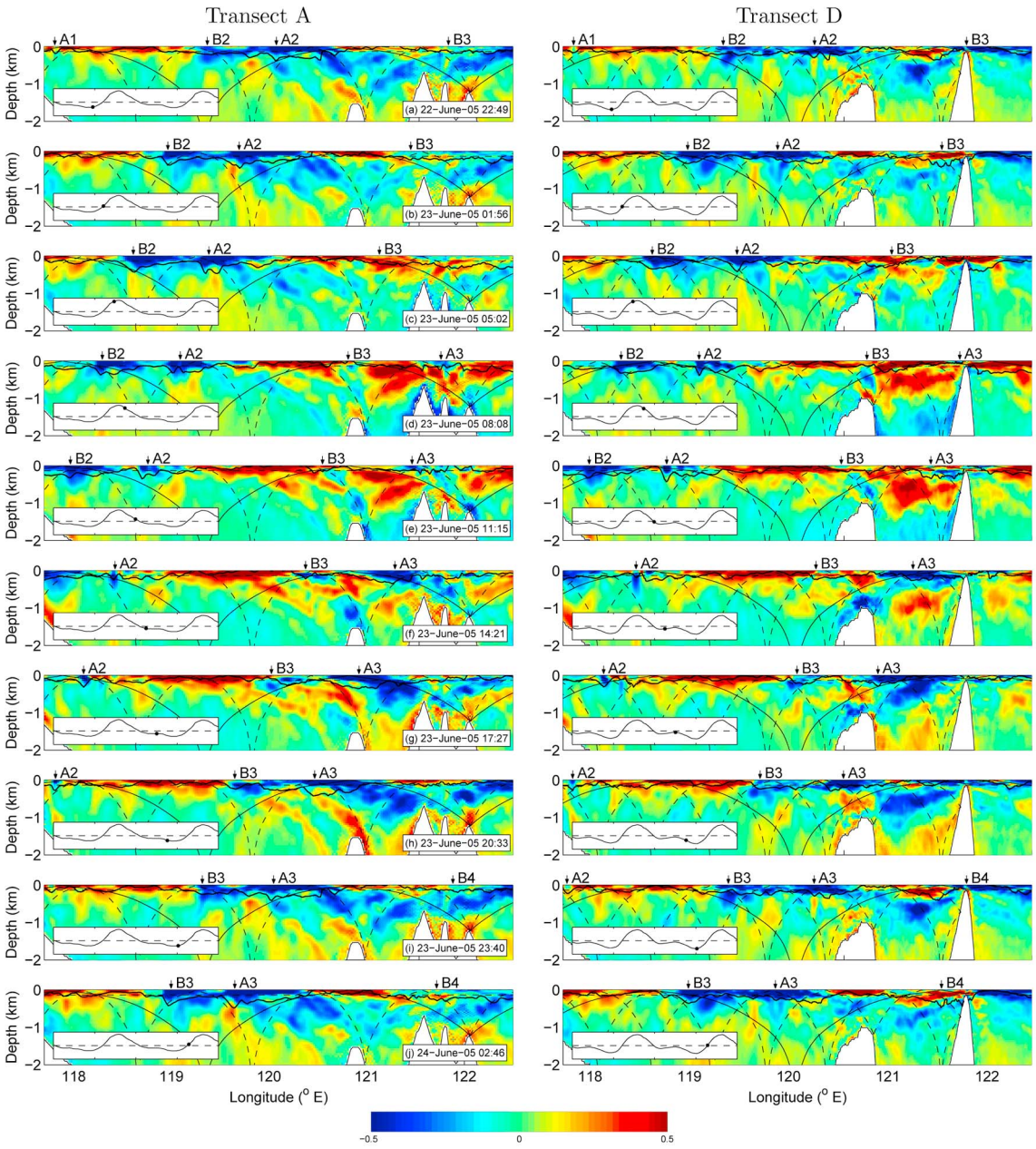

Figure 22. East-west baroclinic velocity field (in m s^{-1}) at intervals of 3.1 h beginning at 2249 on 22 June 2005 showing the evolution of A and B waves along Transects (left) A and (right) D. The time period corresponds to that shown in Figures 9d–9h. The thick solid line shows the 20° isotherm with an amplitude relative to its depth at rest (the horizontal dashed line at −135 m) magnified by a factor of 5. For reference, K_1 internal rays are shown by the solid lines and M_2 rays are dashed. The inset plots depict the east-west barotropic currents at location L2 (Figure 22, left) and L1 (Figure 22, right).

model of generation over sinusoidal topography. We consider a single topographic ridge with bottom height of the form

$$h(x) = \begin{cases} \frac{1}{2}h_0[1+\cos(k_b x)] & |k_b x| < \pi, \\ 0 & \text{otherwise}, \end{cases}$$

where h_0 is the amplitude of the topography and the other parameters are defined in section 4.3. Inviscid barotropic flow over this ridge can be estimated by assuming a rigid lid so that

$$u(x,t) = U_0 \sin(\omega t)\frac{d-h_0}{d-h(x)},$$

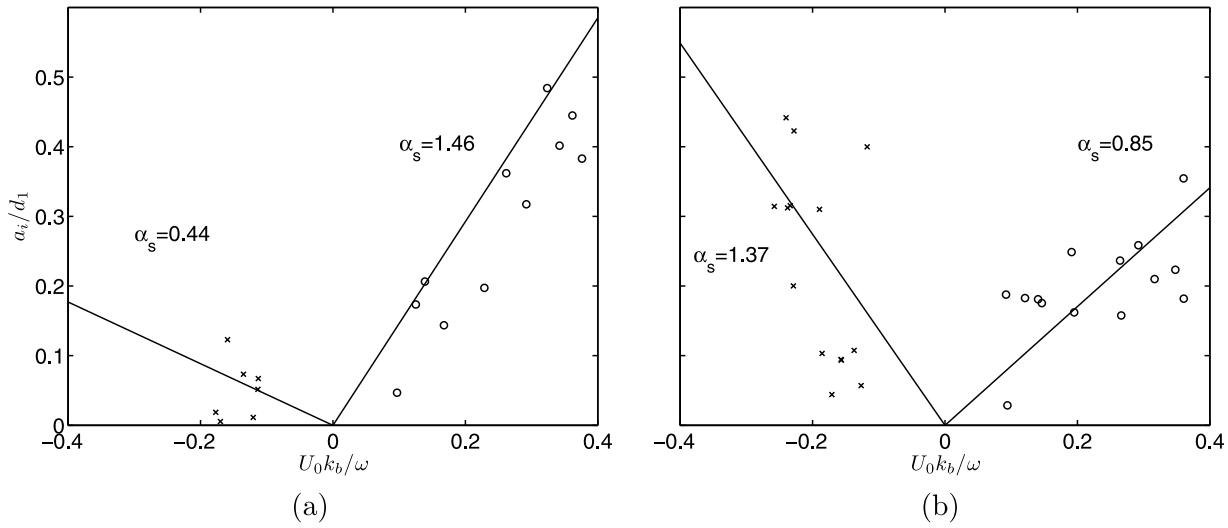

Figure 23. Amplitudes of internal waves (given by the displacement of the 20° isotherm) arriving at locations C1 and C2 for A (circles) and B waves (crosses), compared to the least squares fit to equation (3) via adjustment of the value α_s as indicated. (a) Waves arriving at C1 generated by currents at location L2 and (b) waves arriving at location C2 generated by currents at location L1 are represented. The negative values of U_0k_b/ω imply peak flood (westward) currents which generate B waves.

where d is the depth in the absence of the topography. Assuming a free slip bottom boundary, the barotropic vertical velocity at a depth d_1 is then given by

$$w(x, z = -d_1, t) = u(x,t)h_x \frac{d_1}{d - h(x)}.$$

Further assuming a linear relationship between the isopycnal displacements and the barotropic velocity, such that $w = \partial\zeta/\partial t$, the maximum isopycnal displacement occurs at the location of maximum slope where $h_x = k_b h_0/2$, and is given by

$$\frac{a_i}{d_1} = \epsilon f(\delta), \tag{2}$$

where the excursion parameter is $\epsilon = U_0k_b/\omega$, $\delta = h_0/d$, and

$$f(\delta) = \frac{\delta(1-\delta)}{(1-\delta/2)^2}.$$

This function is maximized at $\delta = 2/3$ where $f_{\max} = 1/2$, and decays to zero at $\delta = 0$ and $\delta = 1$. Since the maximum barotropic current is assumed constant at U_0, then no vertical displacement occurs in the absence of the ridge when $\delta = 0$. The case in which $\delta = 1$ implies infinitely small vertical velocity because there is effectively no volume flux over the ridge. Equation (2) shows that an estimate of the isopycnal displacement is given directly by the excursion parameter, and represents an estimate for the amplitude of a wave emanating from a point source located at the point of maximum slope along the ridge. In reality, waves in the SCS result from a superposition of waves emanating from line sources distributed along complex three-dimensional, multiridge systems. Therefore, the amplitude of the waves is better represented by the expression

$$\frac{a_i}{d_1} = \alpha_s \epsilon. \tag{3}$$

Here, α_s is a constant for fixed topography, while ϵ will vary over the spring-neap cycle as the amplitude of the barotropic currents varies. Due to amplitude dispersion, variable topography along the propagation path, and the superposition of waves, the value of α_s will vary for a given wave as it propagates across the basin. However, at a fixed point in space, the value of α_s can represent variability not captured by the simplicity of equation (3). The variability of the currents that generate the wave and affect its amplitude will be captured by ϵ.

[43] Equation (3) is used to understand the relationship between tidal currents in the Luzon Strait and the internal waves they generate. To correlate A waves with tidal currents at the A ridge, we relate the internal waves that pass by location C1 to the currents at L2 (see Figure 1 for locations). Location C1 is south of Transect B and so should have weak B wave signatures. B waves at location C2 are correlated to tidal currents at L1. Location C2 will also have strong A wave signatures because it lies near the intersection of Transects A and B. For each point in time at which the tidal currents over the ridges at locations L1 and L2 are maximum and eastward, we assume that these currents generate A waves. The maximum westward currents are assumed to generate B waves. The amplitude a_i of the waves is then given by the negative displacement of the 20° isotherm relative to its reference level of d_1 = 135 m. At locations C1 and C2, the amplitudes of the waves associated with the currents at the ridges are determined by shifting the time series of the isotherm displacements backward in time so that the amplitudes of the largest waves line up with the strongest barotropic currents at the associated ridges. The time series at mooring C1 is therefore shifted backward in time by 18 h and that at C2 is shifted by 28 h, reflecting the longer distance from C2 to L1 than from C1 to L2. We assume that the topographic scale at locations L1 and L2 is $k_b = 2\pi/(100$ km) and the characteristic tidal frequencies at L1 and L2 are both semidiurnal.

[44] As shown in Figure 23, despite the simplicity of equation (3), it predicts the amplitude of the internal waves at C1 and C2 quite well. The results show that the internal wave amplitudes at C1 and C2 are linearly proportional to the excursion parameter at their respective ridges. The computed A wave amplitudes at C1 (Figure 23a) have the least scatter relative to the theoretical prediction because the A waves have not yet steepened into weekly nonlinear waves by this point (120°E). Instead, they exist as large-amplitude semidiurnal internal tides. Furthermore, location C1 is minimally influenced by B waves and so they do not interact with or alter the A waves. This is in contrast to location C2 (Figure 23b) which is near the intersection of Transects A and B. At this intersection, large-amplitude A and B waves interact and lead to the scatter in the wave amplitudes at C2. Although strong A waves are generated closer to L2, there is good correlation between A waves at C2 and the tides at L1 because location C2 is relatively close to Transect A and the phasing in the peak eastward currents does not change appreciably as one moves from L1 to L2 (see Figure 20). The reduction in amplitude of A waves from C1 to C2 is consistent with the behavior of the amplitude of the A waves as they propagate west, as discussed with reference to Figure 13. This accounts for the reduced value of α_s for the A waves as they propagate from C1 to C2. The opposite is true for the B waves which increase in magnitude from C1 to C2 thereby requiring an increase in α_s. Although this simplified linear model predicts the amplitude of the waves computed by SUNTANS, it may not accurately predict the behavior of the observed large-amplitude waves (those that exceed 60 m) due to nonlinear effects.

5. Summary and Conclusions

[45] We have presented three-dimensional simulations of internal wave generation and propagation in the SCS. The resolution employed in the simulations is sufficient to resolve the large-scale internal tides as exhibited by the agreement between the observed and computed internal wave arrival times at moorings B1 and S7. Favorable agreement with SAR imagery on the shelf around Dongsha Atoll indicates that the grid resolution is also sufficient to resolve the processes that affect shoaling and wave-wave interaction. The magnitude of the free surface gradient produces the best match between the simulations and the SAR imagery because the free surface gradient highlights regions of horizontal flow convergence or divergence near the surface due to first-mode internal waves. The barotropic currents computed by the model are sufficiently accurate to produce the observed internal tidal wavefield. However, insufficient bathymetric resolution leads to a slight underprediction of the barotropic currents in the Luzon Strait which leads to an underprediction of the internal wave amplitude. The underprediction of the barotropic currents is accompanied by underprediction of the effects of nonlinear steepening due to the relatively coarse resolution in the SCS basin. This effect is further pronounced when the waves shoal onto the continental shelf, where the grid resolution is insufficient to resolve the extent of the observed nonlinear steepening. As a result, model-predicted phase speeds are weakly dependent on the wave amplitude which is in contrast to the observations which indicate strong amplitude dispersion. Despite the underprediction of the wave amplitude, the good agreement between the observed and computed wave arrival times at mooring B1 indicates that the simulated generation and propagation dynamics provide a representative picture of the real system. Although an increase in the grid resolution would yield better insight into the weakly nonlinear processes in the deep basin and on the shelf, the resolution employed in the simulations, which requires roughly 11 million grid cells ($\sim 215^3$), is already unprecedented and represents the highest-resolution simulations of internal waves in the SCS to date.

[46] The simulations reproduce the well-known A and B waves that propagate across the SCS basin. Like the observations, the predictions show that A waves are larger than B waves at mooring B1. This causes dispersion of A waves into rank-ordered wave trains while B waves exist as single, smaller-amplitude peaks. The amplitude of the B waves and the associated dispersion is comparable to that of the A waves after they shoal onto the continental shelf. Further to the south at location B2, B waves are larger than A waves. On the shelf, the signal of A waves is lost as they propagate through the B wave trains. The A waves are larger at B1 and B waves are larger at B2 because location B2 lies in the path of the dominant direction of propagation of B waves. This dominant heading is inferred from the centers of the arcs that form from the cylindrical depression waves in the SCS basin. Although the location of these centers changes over the spring-neap tidal cycle, they remain confined to a particular heading which is obtained with a least squares fit line to the arc centers. The least squares fit lines indicate that A waves propagate predominantly along a heading of 282° while B waves propagate along a heading of 267°. These headings are consistent with the semimajor axes of the tidal current ellipses which are normal to two primary ridges in the Luzon Strait. In the north, the B ridge is normal to the propagation path of the B waves. In the south, the A ridge is normal to the propagation path of the A waves.

[47] The Hovmöller diagram of the isopycnal displacements shows that the internal wavefield in the SCS is composed of a complex network of first- and second-mode internal waves which emanate from the Luzon Strait. These make it difficult to assess phase speeds in some areas because superposition of different modes leads to internal wave peaks in the isotherms that do not propagate. Nevertheless, the Hovmöller diagram clearly shows that, before shoaling on the continental shelf, on average the first-mode A and B waves propagate along characteristic curves that follow the semidiurnal first-mode internal wave speed. This is consistent with observations although observations indicate stronger amplitude dispersion. The simulations show deceleration of the waves as they propagate onto the shelf. However, in contrast to the observations, the onshelf waves propagate more slowly than the linear phase speed. This we hypothesize to result from reflected and locally generated diurnal internal tidal energy. When traced back to the eastern ridge in the Luzon Strait, the first-mode A wave characteristics consistently line up near peak eastward (ebb) barotropic tidal currents. The first-mode B wave characteristics consistently line up with peak westward (flood) currents.

[48] Analysis of the baroclinic velocity fields shows that both A and B waves form throughout the entire north-south

extent of two-ridge system in the Luzon Strait. Westward currents associated with emergent A waves appear in the upper water column during peak ebb tides at the eastern ridge. These currents are associated with beams that emanate from the eastern flanks of the eastern ridge. Westward currents in the upper water column are observed following the A waves as they propagate westward between the ridges. Although emergence of B waves is not as clear, resonance of the semidiurnal internal tide affects B wave propagation because the western ridge is roughly one semidiurnal internal tidal wavelength to the west of the eastern ridge. Semidiurnal resonance is strongest normal to the B ridge because the semidiurnal barotropic tides are stronger than they are at the A ridge, and the western ridge is more prominent west of the B ridge. Therefore, B waves are stronger along the heading of 267° which is normal to the B ridge. A wave generation is stronger to the south and along the A ridge because of semidiurnal-diurnal beam superposition. Deeper eastern ridges coupled with stronger diurnal barotropic tidal currents produce stronger diurnal beams and hence stronger A waves that propagate on a path that is perpendicular to the A ridge. Steepening of the diurnal internal tide is arrested by rotational dispersion which prevents the formation of diurnal solitary-like waves in the SCS basin.

[49] The phasing of the A and B waves depends very weakly on the strength of the tidal currents. Despite the large amplitude of the waves, this implies that the generation mechanism is linear and is not due to the classic lee wave release mechanism. If hydraulic mechanisms resulting from nonlinear processes were important, the phasing of the waves would vary over the spring-neap cycle, since the time at which the flow turns from super- to subcritical, which is the time in which lee waves are "released", would be a strong function of the maximum internal Froude number. Instead, the phasing is predictable as is the internal wave amplitude, which can be evaluated with reasonable accuracy as a linear function of the excursion parameter. This is demonstrated via comparison of the internal wave amplitude along Transect II to linear theory which shows a good match particularly for A waves.

[50] **Acknowledgments.** The authors gratefully acknowledge the support of U.S. Office of Naval Research under grants N00014-05-1-0294 (Zhang and Fringer) and N00014-08-1-0393 (Ramp) which enabled us to be a part of the Nonlinear Internal Wave Initiative (NLIWI) DRI (scientific officers are C. Linwood Vincent, Terri Paluszkiewicz, and Scott Harper). Interaction with NLIWI colleagues was instrumental in formulating many of the ideas in this paper. We thank Matthew Alford, Maarten Buijsman, and Harper Simmons for numerous discussions related to internal wave generation and propagation in the SCS. Maarten Buijsman and two anonymous referees provided numerous comments which significantly improved the quality of the manuscript. Fred Bahr performed the data analysis and quality control for the field program. We also acknowledge the ARL Major Shared Resource Center for the computer time which was obtained as part of a DOD Challenge Allocation. We thank the Ocean Data Bank of the National Center for Ocean Research in Taiwan for providing the bathymetry.

References

Alford, M. H., R.-C. Lien, H. Simmons, J. Klymak, S. Ramp, Y. J. Yang, D. Tang, and M.-H. Chang (2010), Speed and evolution of nonlinear internal waves transiting the South China Sea, *J. Phys. Oceanogr.*, *40*, 1338–1355, doi:10.1175/2010JPO4388.1.

Apel, J. R., J. R. Holbrock, A. K. Liu, and J. J. Tsai (1985), The Sulu Sea internal soliton experiment, *J. Phys. Oceanogr.*, *15*, 1625–1651.

Barad, M. F., and O. B. Fringer (2010), Simulations of shear instabilities in interfacial solitary waves, *J. Fluid Mech.*, *644*, 61–95.

Boyd, J. P. (1995), Microbreaking and polycnoidal waves in the Ostrovsky-Hunter equation, *Phys. Lett. A.*, *338*, 36–43.

Buijsman, M. C., J. C. McWilliams, and C. R. Jackson (2010a), East-west asymmetry in nonlinear internal waves from Luzon Strait, *J. Geophys. Res.*, *115*, C10057, doi:10.1029/2009JC006004.

Buijsman, M. C., Y. Kanarska, and J. C. McWilliams (2010b), On the generation and evolution of nonlinear internal waves in the South China Sea, *J. Geophys. Res.*, *115*, C02012, doi:10.1029/2009JC005275.

Cai, S., X. Long, and Z. Gan (2002), A numerical study of the generation and propagation of internal solitary waves in the Luzon Strait, *Oceanol. Acta*, *25*, 51–60.

Chao, S.-Y., D.-S. Ko, R.-C. Lien, and P.-T. Shaw (2007), Assessing the west ridge of Luzon Strait as an internal wave mediator, *J. Oceanogr.*, *63*, 897–911.

Chapman, D. C., D.-S. Ko, and R. H. Preller (2004), A high-resolution numerical modeling study of the subtidal circulation in the northern South China Sea, *IEEE J. Oceanic Eng.*, *29*, 1087–1104.

Du, T., Y.-H. Tseng, and X.-H. Yan (2008), Impacts of tidal currents and Kuroshio intrusion on the generation of nonlinear internal waves in Luzon Strait, *J. Geophys. Res.*, *113*, C08015, doi:10.1029/2007JC004294.

Duda, T. F., J. F. Lynch, R. C. Beardsley, J. D. Irish, S. R. Ramp, C. S. Chiu, T. Y. Tang, and Y. J. Yang (2004), Internal tide and nonlinear internal wave behavior at the continental slope in the northern South China Sea, *IEEE J. Oceanic Eng.*, *29*, 1105–1130.

Ebbesmeyer, C. C., C. A. Coomes, R. C. Hamilton, K. A. Kurrus, T. C. Sullivan, B. L. Salem, R. D. Romea, and R. J. Bauer (1991), New observations on internal waves (solitons) in the South China Sea using an acoustic Doppler current profiler, *Proc. Mar. Technol. Soc.*, *91*, 165–175.

Egbert, G. D., and S. Y. Erofeeva (2002), Efficient inverse modeling of barotropic ocean tides, *J. Atmos. Oceanic Technol.*, *19*, 183–204.

Farmer, D. M., and J. D. Smith (1980), Tidal interaction of stratified flow with a sill in Knight Inlet, *Deep Sea Res. Part A*, *27*, 239–246.

Farmer, D., Q. Li, and J.-H. Park (2009), Internal wave observations in the South China Sea: The role of rotation and non-linearity, *Atmos.-Ocean*, *47*, 267–280.

Fringer, O. B., M. Gerritsen, and R. L. Street (2006), An unstructured grid, finite-volume, nonhydrostatic, parallel coastal ocean simulator, *Ocean Modell.*, *14*, 139–278, doi:10.1016/J.OCEMOD.2006.03.006.

Garrett, C., and E. Kunze (2007), Internal tide generation in the deep ocean, *Ann. Rev. Fluid Mech.*, *39*, 57–87.

Gerkama, T. (1996), A unified model for the generation and fission of internal tides in a rotating ocean, *J. Mar. Res.*, *54*, 421–450.

Harten, A. (1983), High resolution schemes for hyperbolic conservation laws, *J. Comput. Phys.*, *49*, 357–393.

Helfrich, K. R. (2007), Decay and return of internal solitary waves with rotation, *Phys. Fluids*, *19*, 026601, doi:10.1063/1.2472509.

Hsu, M.-K., and A. K. Liu (2000), Nonlinear internal waves in the South China Sea, *Can. J. Remote Sens.*, *26*, 72–81.

Hsu, M.-K., A. K. Liu, and C. Liu (2000), A study of internal waves in the China Seas and Yellow Sea using SAR, *Cont. Shelf Res.*, *20*(4), 389–410.

Jachec, S. M. (2007), Understanding the evolution and energetics of internal tides within Monterey Bay via numerical simulations, Ph.D. dissertatation, Stanford Univ., Stanford, Calif.

Jachec, S. M., O. B. Fringer, M. G. Gerritsen, and R. L. Street (2006), Numerical simulation of internal tides and the resulting energetics within Monterey Bay and the surrounding area, *Geophys. Res. Lett.*, *33*, L12605, doi:10.1029/2006GL026314.

Jackson, C. R. (2009), An empirical model for estimating the geographic location of nonlinear internal solitary waves, *J. Atmos. Oceanic Tech.*, *26*, 2243–2255.

Jackson, C. R., and J. R. Apel (2004), *An Atlas of Internal Solitary-Like Waves and Their Properties*, 2nd ed., Global Ocean Assoc., Alexandria, Va. (Available at http://www.internalwaveatlas.com/.)

Jan, S., R.-C. Lien, and C.-H. Ting (2008), Numerical study of baroclinic tides in Luzon Strait, *J. Oceanogr.*, *64*, 789–802.

Johnston, T. M. S., M. A. Merrifield, and P. E. Holloway (2003), Internal tide scattering at the Line Islands ridge, *J. Geophys. Res.*, *108*(C11), 3365, doi:10.1029/2003JC001844.

Kunze, E. (1985), Near-inertial wave propagation in geostrophic shear, *J. Phys. Oceanogr.*, *15*, 544–565.

Lansing, F. S., and T. Maxworthy (1984), On the generation and evolution of internal gravity waves, *J. Geophys. Res.*, *99*, 843–864.

Laurent, L. S., and C. Garrett (2002), The role of internal tides in mixing the deep ocean, *J. Phys. Oceanogr.*, *32*, 2882–2899.

Lien, R.-C., T. Y. Tang, M. H. Chang, and E. A. D'Asaro (2005), Energy of nonlinear internal waves in the South China Sea, *Geophys. Res. Lett.*, *32*, L05615, doi:10.1029/2004GL022012.

Liu, A. K., and M. K. Hsu (2004), Internal wave study in the South China Sea using Synthetic Aperture Radar (SAR), *Int. J. Remote Sens.*, *25*, 1261–1264.

Liu, A. K., J. R. Holbrook, and J. R. Apel (1985), Nonlinear internal wave evolution in the Sulu Sea, *J. Phys. Oceanogr.*, *15*, 1613–1624.

Liu, A. K., S. R. Ramp, Y. Zhao, and T. Y. Tang (2004), A case study of internal solitary wave propagation during ASIAEX 2001, *IEEE J. Oceanic Eng.*, *29*, 1144–1156.

Lynett, P. L., and P. L.-F. Liu (2002), A two-dimensional, depth-integrated model for internal wave propagation over variable bathymetry, *Wave Motion*, *26*, 221–240.

Maxworthy, T. (1979), A note on internal solitary waves produced by tidal flow over a three dimensional ridge, *J. Geophys. Res.*, *84*, 338–346.

Niwa, Y., and T. Hibiya (2004), Three-dimensional numerical simulation of M_2 internal tides in the East China Sea, *J. Geophys. Res.*, *109*, C04027, doi:10.1029/2003JC001923.

Pawlowicz, R., B. Beardsley, and S. Lentz (2002), Classical tidal harmonic analysis including error estimates in MATLAB using T_TIDE, *Comput. Geosci.*, *28*, 929–937.

Peacock, T., M. J. Mercier, H. Didelle, S. Viboud, and T. Dauxois (2009), A laboratory study of low-mode internal tide scattering by finite-amplitude topography, *Phys. Fluids*, *21*, 121702, doi:10.1063/1.3267096.

Rainville, L., T. M. S. Johnston, G. S. Carter, M. A. Merrifield, R. Pinkel, P. F. Worcester, and B. D. Dushaw (2010), Interference pattern and propagation of the M2 internal tide south of the Hawaiian Ridge, *J. Phys. Oceanogr.*, *40*, 311–325.

Ramp, S. K., T. Y. Tang, T. F. Duda, J. F. Lynch, A. K. Liu, C. S. Chiu, F. L. Bahr, H. R. Kim, and Y. J. Yang (2004), Internal solitons in the northwestern South China Sea. Part I: Sources and deep water propagation, *IEEE J. Oceanic Eng.*, *29*, 1157–1181.

Ramp, S. R., Y. J. Yang, and F. L. Bahr (2010), Characterizing the nonlinear internal wave climate in the northeastern South China Sea, *Nonlinear Processes Geophys.*, *17*, 481–498.

Roe, R. E. (1985), Some contributions to the modeling of discontinuous flows, *Lect. Appl. Math.*, *22*, 163–193.

Shaw, P.-T., D. Ko, and S.-Y. Chao (2009), Internal solitary waves induced by flow over a ridge: With applications to the northern South China Sea, *J. Geophys. Res.*, *114*, C02019, doi:10.1029/2008JC005007.

Simmons, H. L., R. W. Hallberg, and B. K. Arbic (2004), Internal wave generation in a global baroclinic tide model, *Deep Sea Res. Part II*, *51*, 3043–3068.

Vlasenko, V., N. Stashchuk, and K. Hutter (2005), *Baroclinic Tides Theoretical Modeling and Observational Evidence*, 351 pp., Cambridge Univ. Press, New York.

Zhang, Z. (2010), Numerical simulations of nonlinear internal waves in the South China Sea, Ph.D. dissertation, Stanford Univ., Stanford, Calif.

Zhang, Z., and O. B. Fringer (2006), A numerical study of nonlinear internal wave generation in the Luzon Strait, in *Proceedings of the* 6th *International Symposium on Stratified Flows*, edited by G. N. Ivey, pp. 300–305, Univ. of West. Aust., Perth, West. Aust., Australia.

Zhao, Z., and M. H. Alford (2006), Source and propagation of internal solitary waves in the northeastern South China Sea, *J. Geophys. Res.*, *111*, C11012, doi:10.1029/2006JC003644.

Zhao, Z., V. Klemas, Q. Zheng, and X.-H. Yan (2004), Remote sensing evidence for baroclinic tide origin of internal solitary waves in the northeastern South China Sea, *Geophys. Res. Lett.*, *31*, L06302, doi:10.1029/2003GL019077.

O. B. Fringer and Z. Zhang, Environmental Fluid Mechanics Laboratory, Department of Civil and Environmental Engineering, Stanford University, 473 Via Ortega, Stanford, CA 94305, USA. (fringer@stanford.edu; zhonghua@stanford.edu)

S. R. Ramp, Monterey Bay Aquarium Research Institute, 7700 Sandholdt Rd., Moss Landing, CA 95039-9644, USA. (sramp@mbari.org)